Starch Capped Atomically Thin CuS Nanocrystals for Efficient Photothermal Therapy

Zheng, Zhiyong; Yu, Ping; Cao, Huili; Cheng, Mengyu; Zhou, Thomas; Lee, Li E.; Ulstrup, Jens; Zhang, Jingdong; Engelbrekt, Christian; Ma, Lixin

Published in:
Small

Link to article, DOI:
10.1002/smll.202103461

Publication date:
2021

Document Version
Early version, also known as pre-print

Link back to DTU Orbit

Citation (APA):
Zheng, Z., Yu, P., Cao, H., Cheng, M., Zhou, T., Lee, L. E., Ulstrup, J., Zhang, J., Engelbrekt, C., & Ma, L. (2021). Starch Capped Atomically Thin CuS Nanocrystals for Efficient Photothermal Therapy. *Small*, *17*(47), Article 2103461. https://doi.org/10.1002/smll.202103461

Starch Capped Atomically Thin CuS Nanocrystals for Efficient Photothermal Therapy

Zhiyong Zheng, Ping Yu, Huili Cao, Mengyu Cheng, Thomas Zhou, Li E. Lee, Jens Ulstrup, Jingdong Zhang[†]*, Christian Engelbrekt*, and Lixin Ma**

Dr. Z. Zheng, Dr. H. Cao, Prof. J. Ulstrup, Prof. J. Zhang, Dr. C. Engelbrekt
Department of Chemistry
Technical University of Denmark,
Kgs. Lyngby 2800, Denmark
E-mail: cheng@kemi.dtu.dk

Prof. P. Yu, Dr. L. E. Lee
Department of Physics and Astronomy
University of Missouri
Columbia, Missouri 65211, United States

Dr. M. Cheng
Department of Pulmonary and Critical Care Medicine
Shanxi Bethune Hospital
Taiyuan 030001, P. R. China

Dr. M. Cheng, T. Zhou, Dr. L. E. Lee, Prof. L. Ma
Department of Radiology
University of Missouri
Columbia, Missouri 65212, United States
& Research Division/Biomolecular Imaging Center
Harry S. Truman Memorial Veterans' Hospital
Columbia, Missouri 65201, United States
E-mail: mal@health.missouri.edu

[†]Deceased in January 2020

Keywords: copper sulfides, starch, photothermal therapies, localized surface plasmon resonances, photothermal effects, nanocrystals, finite element method

Photothermal therapy requires efficient plasmonic nanomaterials with small size, good water dispersibility, and biocompatibility. This work reports a one-pot, two-minute synthesis strategy for ultrathin CuS nanocrystals (NCs) with precisely tunable size and localized surface plasmon resonance (LSPR), where a single-starch-layer coating leads to a high LSPR absorption at the near-infrared wavelength 980 nm. The CuS NC diameter increases from 4.7 nm (1 nm height along [101]) to 28.6 nm (4.9 nm height along [001]) accompanied by LSPR redshift from 978 to 1200 nm, as the precursor ratio decreases from 1 to 0.125. Photothermal temperature elevates by 38.6 °C in 50 mg L^{-1} CuS NC solution under laser illumination (980 nm, 1.44 W cm^{-2}). Notably, 98.4% of human prostate cancer PC-3/Luc+ cells are killed by as little as 5 mg L^{-1} starch-coated CuS NCs with 3-minute laser treatment, whereas CuS NCs without starch cause insignificant cell death. LSPR modeling discloses that the starch layer enhances the photothermal effect by significantly increasing the free carrier density and blue-shifting the LSPR towards 980 nm. Our study not only presents a new type of photothermally highly efficient ultrathin CuS NCs, but also offers in-depth LSPR modeling investigations useful for other photothermal nanomaterial designs.

1. Introduction

Photothermal therapy (PTT) is a minimally-invasive therapeutics in oncology for tumor treatment by converting light to heat triggering cell death.[1, 2] With the widespread availability of laser therapy devices in clinics, PTT attracts increasing interests of clinicians and patients due to its promising potential for effective treatment and minimized side effects.[3-5] However, advance of PTT for adoption in clinical cancer treatment is hampered to date by the limited success in the development of clinical photothermal therapy agents.[6] PTT exploits heat generated locally by a photosensitizer,[7] in which both the photothermal agents and laser sources, as well as the matching between them, are essential. Laser thermal therapy generally employs continuous-wave lasers with wavelengths of either 808 or 980 nm.[8, 9] The wavelengths are in the near-infrared (NIR, λ = 700-1100 nm) window so that photons can penetrate deep into biological tissue.[10-12] Certain nanoparticles (NPs) have proper carrier densities enabling them to exhibit localized surface plasmon resonances (LSPRs) that efficiently facilitate the conversion of NIR light into heat.[10-12]

Several types of NPs are currently being developed as photosensitizers, including metallic and semiconductor NPs. Noble metal NPs, e.g., Ag and Au NPs, have been extensively applied for the LSPRs in the visible spectrum.[5, 13-15] Semiconductor NPs have tunable carrier concentration and LSPRs typically in the NIR range.[10, 11] A high photothermal conversion efficiency is key to effective NP photosensitizers to avoid thermal damage to healthy tissue, which is a serious problem in PTT. The NPs with a high photothermal conversion efficiency and tumor selectivity can thus effectively destroy the cancer cells at a low photon density and in a short treatment time, while keeping the surrounding healthy tissue at a safe temperature.[16] Other key factors to consider for developing photosensitizers are NP size and surface chemistry. The NPs must be small so that they can be injected into the bloodstream, delivered to the tumor sites, and excreted through the renal and hepatic systems.[17] Accumulation of NPs in tumor tissue can occur by active targeting the tumor cells after NPs functionalization with ligands, or *via* passive targeting due to the enhanced permeability and retention effect in the tumor tissue.[18] NPs with hydrophilic and neutral or slightly anionic surface are preferred for tumor tissue targeting. Leaky tumor blood vessels thus allow enhanced permeation of NPs to tumor stroma, while absence of normal lymphatic drainage in the tumor contributes to the NP retention. With such considerations, small semiconductor nanomaterials are good candidates for PTT.

Mixed-valence copper sulfides ($Cu_{2-x}S$, $0 \leq x \leq 1$) are unique p-type semiconductors and have attracted significant attention in photothermal therapy.[19] Copper sulfides are cost-friendly compared to noble metals and have different crystal phases ranging from chalcocite (Cu_2S) to covellite (CuS).[19] The carrier concentration of copper sulfides increases with increasing number of Cu vacancies (x),[20, 21] so CuS possesses the highest carrier concentration among copper sulfides. In CuS, copper ions bind tetrahedrally and trigonally with sulfide ions, and covalent bonds (S–S) bind two sulfide ions.[22] In some cases, the anisotropic crystal structure of CuS leads to 2D growth perpendicular to the z-axis and a layered structure,[23] probably due to the dissimilar surface energies of {110} and {001} facets.[24] The CuS band gap ranges from 1.1 to 2.0 eV depending on the crystal phase and composition.[10] The LSPR of CuS is tunable and depends further on the CuS NP size. LSPR peaks of CuS nanoplatelets synthesized in oleylamine shifted from around 1030 to 1640 nm when the lateral size increased from 7.5 to 34 nm.[10] CuS finally showed low cytotoxicity where cell viability maintained after treatment with CuS nanoplates at Cu concentrations below 100 mg L^{-1}.[25] With a similar size, hollow CuS NPs and hollow gold nanospheres showed disparate biodegradability. In contrast to the nonmetabolizable hollow gold nanospheres, the hollow CuS NPs can be disassembled into small and biodegradable CuS fragments. Within one-month post-injection, about 90% of the hollow CuS NPs were thus excreted through liver and kidney in mice, while only 3.98% of the hollow gold nanospheres were excreted.[26]

With the low cost, low toxicity, and tunable photothermal properties, CuS has already emerged as a highly promising photothermal agent. For example, flower-like CuS superstructures with diameters from 500 to 800 nm have been used as a photothermal agent for cancer cell ablation, and with the administration of these CuS superstructures, cancer cells in mice were efficiently killed with 980 nm laser treatment.[8] However, the previously reported CuS nanomaterials have limitations such as low photothermal conversion efficiency, demanding synthesis (long duration, high temperature and pressure, toxic chemicals, *etc*.), typically large size, and poor water dispersibility.[7, 8] These limitations hinder their clinical use in PTT.

Herein, we report a simple, two-minutes microwave-assisted synthesis of atomically thin CuS nanocrystals (NCs). As a strategic step, the NCs are coated by a starch layer for potentially enhanced biocompatibility, water dispersibility, and aqueous stability, as well as for efficient photothermal ablation of cancer cells. The tunable size of the CuS NCs is controlled by the precursor ratio Cu:AS (Cu(II): ammonium sulfide). The starch-capped ultrasmall CuS NCs (4.7 nm diameter and 1 nm height) show a distinct crystal structure from the large CuS NCs and are also the thinnest CuS NCs reported so far. A high photothermal ablation efficacy is demonstrated by in vitro treatment of human prostate cancer PC-3/Luc+ cells, where 98.4% cells are killed by as low as 5 mg L^{-1} starch-coated CuS NCs and CuS NCs without starch cause insignificant cell death. Three-dimensional full-wave time-harmonic field analysis discloses that the starch coating enhances the photothermal efficiency of CuS NCs by increasing the free carrier density by up to 3 times, and blue-shifting in-plane LSPR to be dominant at 980 nm. In addition, the free carrier densities are higher in small CuS NCs than large CuS NCs due to their structural differences. Consequently, the in-plane LSPR of small starch-coated CuS NCs perfectly matches the laser wavelength (980 nm) and makes them highly efficient photothermal agents. The study offers insights into the correlation of the plasmonic behavior, the free carrier concentration, and the crystalline structure, and guides the design of PTT agents.

2. Results and Discussion

2.1. Structure of CuS NCs

2.1.1 Structural and Spectral Characterization of CuS NCs

The impact of non-covalent and biocompatible short starch oligomer capping on the CuS nanostructure was studied in detail. The soluble starch used in this work was produced by treatment at 190 °C (a method first studied by Zulkowsky in the 1880s[27, 28]). The stability of starch during the microwave treatment is supported by the near identical UV-vis spectra before and after this process (Figure S1). CuS NCs with and without starch capping showed distinct morphologies. For example, M11-130 NCs (synthesized from 1 mM Cu(II) and 1 mM ammonium sulfide at 130 °C - sample codes are described in the Experimental Section) were small and uniform in size (**Figure 1**A), with a diameter of 4.7 ± 0.9 nm (average lateral diameter unless otherwise stated, Figure 1C and Figure S2H) and of round or irregular shape from top-view. In contrast, M11-130-0 NCs (i.e., the analog of M11-130 without starch coating) were found to be larger and polydisperse (Figure 1B), with diameters of 12.4 ± 4.3 nm (Figure S3 and Figure S4F) and hexagonal shape (Figure 1B). The presence of starch, being the only difference during the syntheses, clearly stabilized small and uniform CuS NCs.

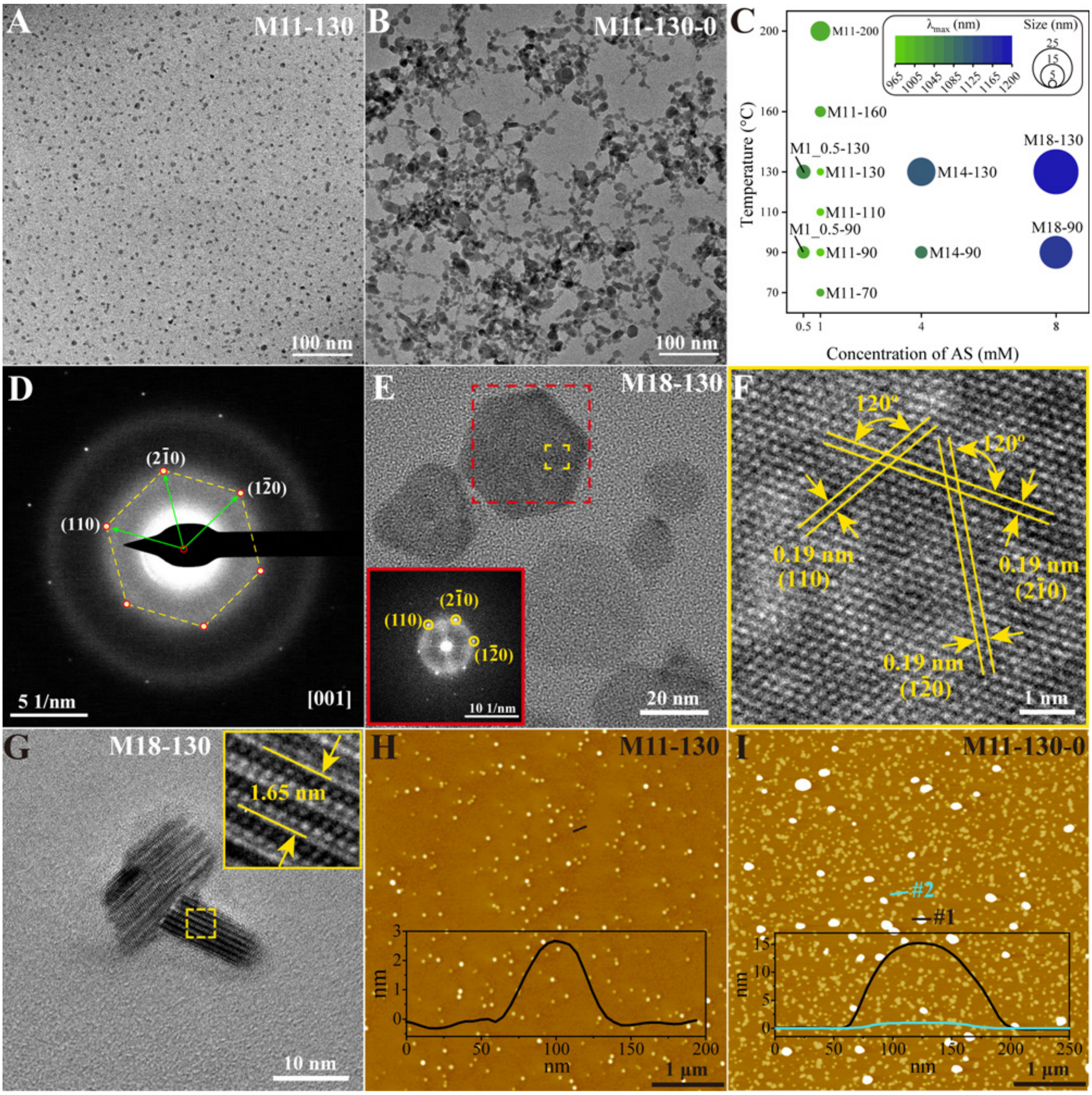

Figure 1. Morphology of CuS NCs. TEM images of (A) M11-130 and (B) M11-130-0. (C) Effect of ammonium sulfide (AS) concentration and synthesis temperature on the size and wavelength of maximum absorbance (λ_{max}) of CuS NCs. The size, represented by the average diameter, is obtained from the fitting of the crystal size distribution of CuS NCs in TEM (Figure S2). λ_{max} was obtained from UV-vis spectra. (D) Selected area electron diffraction (SAED) pattern of a single large CuS NC. (E) Top-view TEM of large CuS NCs showing hexagonal

shape. Insert: fast Fourier transform of the red square area. (F) High-resolution TEM (HRTEM) of the yellow square area in (E) showing lattice spacings of 0.19 nm and interplanar angles of 120°. (G) Side-view TEM of large CuS NCs showing the structure perpendicular to the [001] direction. Insert: HRTEM of the yellow square area with lines indicating the distance between (001) planes. AFM topography images and typical cross-section analyses of CuS NCs synthesized at 130 °C (H) with starch and (I) without starch. The black line in (H) indicates 2.8 nm height of a single CuS NC with a starch coating (M11-130). The cyan line in (I) indicates 1 nm height of a single CuS NC without starch coating (M11-130-0) and the black line 15 nm height of M11-130-0 aggregate.

The ratio of Cu to ammonium sulfide (Cu:AS) significantly affected the CuS NC size. The diameter of the CuS NCs synthesized at 90 °C decreased from 8.0 to 5.1 nm when the Cu:AS ratio decreased from 2 to 1 (M1_0.5-90 vs. M11-90) (Figure 1C and Figure S4A). Decreasing the Cu:AS ratio further led to a monotonous increase of diameter to 20.7 nm at Cu:AS = 8 (M18-90). A similar trend was observed for CuS NCs synthesized at 130 °C, where the diameter reached a minimum of 4.7 nm at Cu:AS = 1 (M11-130) and then increased to 28.6 nm when the ratio was decreased to 0.125 (M18-130) (Figure 1C and Figure S4A). When Cu and AS concentrations were kept the same and increased in parallel, the effect on size was similar, as when the Cu concentration was fixed at 1 mM, indicating that Cu did not limit the NC formation/growth. The size was constant below 2.0 mM (a slight change from 4.7 to 4.9 nm), while it followed a linear increase to 19.6 nm when concentrations were increased to 10.0 mM (Figure S3 and Figure S4A). Synthesis temperature only showed a minor effect on the size. At

Cu:AS = 1, the diameter remained constant at about 5 nm when the synthesis temperature varied from 70 °C to 130 °C, from where the diameter started to increase reaching 12.6 nm at 200 °C (the starch is possibly unstable at 200 °C). Notably, the temperature effect was larger at an intermediate Cu:AS. For example, the diameter doubled from 8.0 to 16.0 nm when the temperature changed from 90 °C to 130 °C at Cu:AS = 0.25 (Figure 1C and Figure S4B).

The detailed structure of CuS NCs was further examined. Atomically resolved transmission electron microscopy (TEM) images of small starch-coated CuS NCs were difficult to obtain due to the amorphous starch layer. Hence, the lattice structure of small CuS NCs without starch coating was studied as a reference. TEM images of small CuS NCs without starch showed individual NCs with different zone axes, i.e., $[1\bar{1}1]$, $[3\bar{1}1]$, [301], [221], $[2\bar{1}1]$, and [101], and other individual NCs with lattice spacings of 0.27 nm belonging to (006) planes (Figure S5). The angles between the six zone axes are summarized in Table S1. All crystals are very close in orientation except for one with zone axis [221], which is therefore unlikely to be representative. The SAED pattern of a single 20 nm CuS NC showed an array of reflections with hexagonal symmetry, indexed to (110), $(2\bar{1}0)$ and $(1\bar{2}0)$ of CuS (Figure 1D)[29] The detailed atomic structure of large CuS NCs was observed by HRTEM, which showed clear hexagonal shapes with indexes of (110), $(2\bar{1}0)$ and $(1\bar{2}0)$ and a lattice spacing of 0.19 nm (Figure 1E–F). The resolved atomic lattices and indexed fast Fourier transform of a single nanoparticle micrograph confirmed that CuS NCs were single-crystalline CuS, according well with the SAED. A side-view of individual large NCs showed a height of more than 5 nm and a periodical contrast pattern with a spacing of 1.65 nm (Figure 1G).

The height of the small CuS NCs was determined by atomic force microscopy (AFM). The CuS NCs were well dispersed on the hydrophilic mica wafer. The morphology of M11-130 was uniform with a typical height of 2.8 nm, including the starch coating (Figure 1H). When starch was excluded from the synthesis (i.e., M11-130-0), the height of most of the prepared CuS NCs dropped to 1 nm, with some CuS NCs of height 5 to 20 nm, Figure 1I. Considering the similarity of M11-130 and M11-130-0, it can be inferred that the surface layer of starch in M11-130 is about 0.9 nm thick. The typical structure of the starch obtained from the Zulkowsky method is a single glucose oligomer with around 12 units and less than two branching points.[30] The starch chain is approximately 0.7 nm in diameter without considering branches or the effect of dehydration. A single layer of starch therefore coated the CuS NCs surface. Owing to the excellent water dispersibility, AFM images of concentrated M11-130 still displayed individual crystals after drying, while M11-130-0 aggregated on the mica wafer (Figure S7). Remarkably, the ultrasmall size of the CuS NCs, especially the 1 nm height paired with 4.7 nm width is unprecedented for CuS nanomaterials. Previously reported CuS nanomaterials are normally a few nanometers in height, for example, 3.2 nm and 4.0 nm among the thinnest.[10, 31] The 1 nm atomic height in the small CuS NCs is possible due to the rapid two-minute synthesis.

Thermal gravimetric analysis (TGA) was applied to determine the CuS:starch mass ratio in M11-130. The gradual mass loss of 6.4% of M11-130 from 25 to 142 °C was due to moisture loss.[32] The further mass loss from 140 to 700 °C arose from the decomposition of starch and CuS confirmed by the reference TGA traces of M11-130-0 (CuS NCs without starch coating) and pure starch (Figure S8). The mass percentage of starch in M11-130 was estimated to be 64%.

The samples with different morphologies were further examined by X-ray Diffraction (XRD). An impurity ($CuSO_4 \cdot 5H_2O$) present in M11-130-0 (**Figure 2**A) and M11-70 (Figure S9) may result from partial oxidation of the CuS nanocrystals.[33-39] The other samples showed pure CuS. The broad peaks confirmed the small crystallite size of CuS NCs observed with TEM. Different sample crystal textures were seen in the diffraction patterns from CuS NCs from different synthesis conditions. Dominant XRD signals were found at a 2θ from 26 to 36°, attributed to (011), (012), (013), and (006) crystal planes, and at about 48.3°, attributed to (110). Notably, the relative XRD peak intensity at 26–36° decreased and the peak at 48.3° sharpened for samples with larger CuS NCs, such as M18-90 and M18-130, compared to other CuS NCs with smaller size such as M11-130 and M11-110 (Figure S9). A similar peak increase and sharpening at 48° was reported for CuS nanoplates when the lateral size increased from 4.3 to 34 nm.[10]

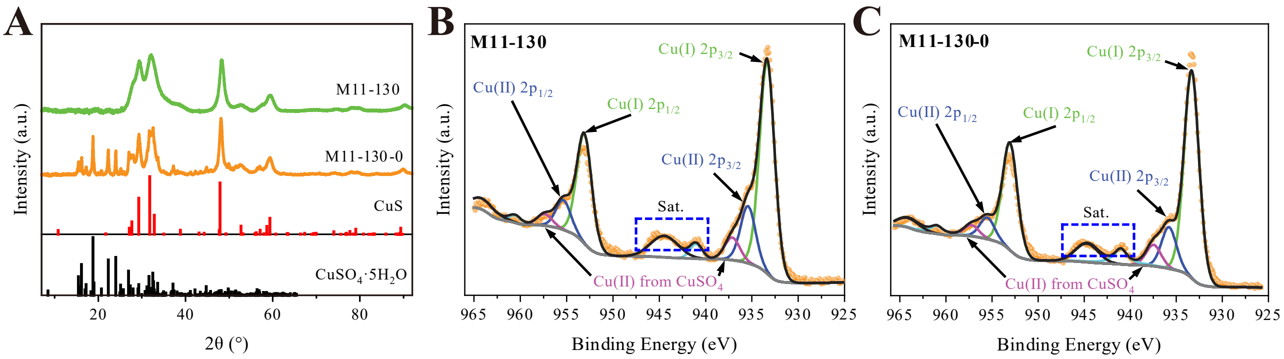

Figure 2. Structure of CuS NCs. (A) XRD patterns of CuS NCs in M11-130 and M11-130-0. Bragg reflections are included for covellite (CuS, COD 96-900-0524, COD ID: 9000523, red bars)[40] and chalcanthite ($CuSO_4 \cdot 5H_2O$, ICOD 01-072-2355, black bars). XRD patterns of

other typical CuS NCs are shown in Figure S9. High-resolution Cu 2p XPS of (B) M11-130 and (C) M11-130-0.

The oxidation state of copper in M11-130 (representing CuS NCs with starch) was investigated by X-ray photoelectron spectroscopy (XPS). An intense doublet appeared at 932.7/952.5 eV in the high-resolution XPS of CuS NCs with starch, attributed to Cu(I) 2p,[41, 42] while two low-intensity doublets at 935.4 and 937.2 eV were attributed to Cu(II) 2p (Figure 2B).[41] It is known that CuS can be transformed to $CuSO_4$ in humid environments,[39] and the doublet at 937.2 eV in fact accords with $CuSO_4$, as confirmed by the result in Figure S10. The satellite peaks (blue box in Figure 2B) further confirm the presence of Cu(II).[41, 43, 44] The XPS spectrum of CuS NCs without starch is similar to that of CuS NCs with starch, and both Cu(I) and Cu(II) were detected (Figure 2C).

2.1.2. Structure of Small and Large CuS NCs and Role of Starch Envelope

The starch-coated CuS NCs in the current study display two typical morphologies. The small CuS NCs (e.g., M11-130 and M11-110, Figure S2H and Figure 1H) are about 1 nm in height and about 5 nm in lateral dimension, while the large CuS NCs are about 5 nm in height with a lateral extension of up to 70 nm. We have shown that the large CuS NCs are of hexagonal covellite crystal structure. The CuS unit cell and corresponding parameters are shown in **Figure 3**A. Apart from the zone axes observed in TEM, Figure S5, four low-index zone axes ([001], [100], [010], and [110]) were considered. The angles between these zone axes are summarized in Table S2. The angles between [100], [010], and [110] and the observed zone axes are quite large (65.5–103.3°), hence these three potential zone axes were excluded. The potential zone axes [001] showed a moderate rotation angle (27.7 ± 9.7°), but these were not observed as perfectly hexagonal fast Fourier transform patterns with lattice spacings of 2.8 Å as would be expected if [001] was the zone axis. Moreover, individual CuS NCs with clear (006) planes in lateral dimension were observed, indicating that the CuS NCs possibly extend along a direction close to the *c* axis. [001] is therefore not the common zone axis of the small CuS NCs. On the other hand, [001] is determined to be the zone axis of the large CuS NCs, see below and as reported for other CuS nanoplates.[10, 45] Considering the similar synthesis conditions, the zone axes of the small and large CuS NCs are expected to be close with small angles between them. Among the six zone axes observed, zone axis [101] is closest to zone axis [001] (13.1°, Table S2) and shows only a small deviation from other zone axes observed (20.5 ± 5.4°, Table S1). [101] is thus proposed as the zone axis of the small CuS NCs and the corresponding structure is shown in Figure 3B.

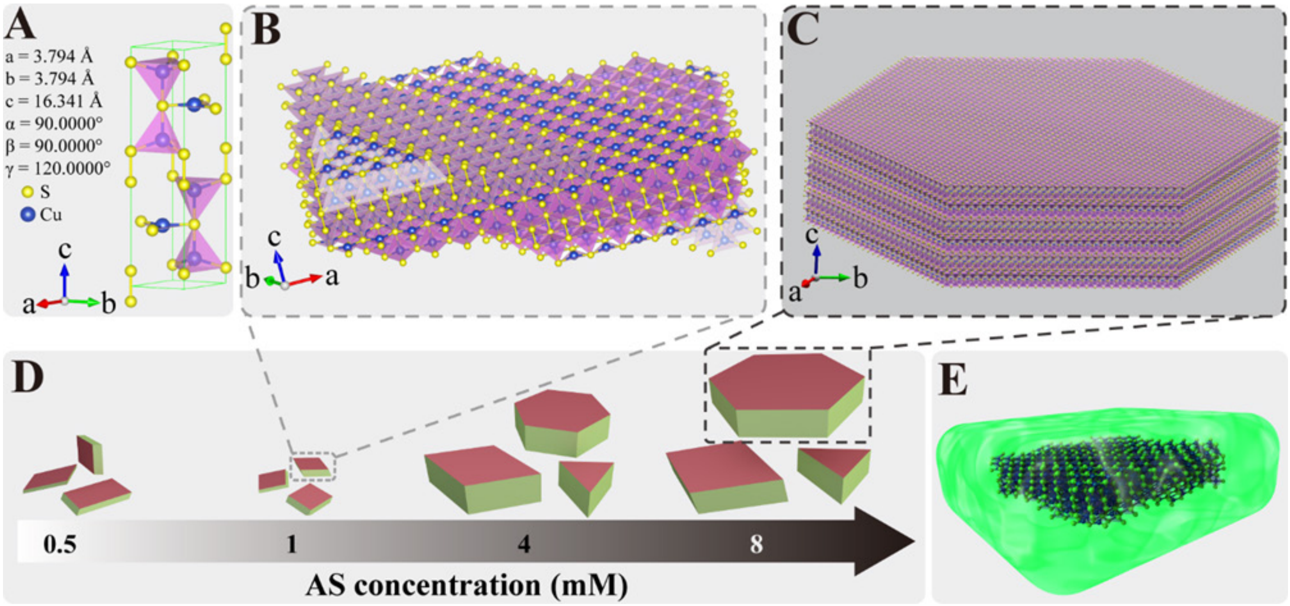

Figure 3. Structural scheme of CuS NCs. (A) A unit cell of CuS. (B) Small CuS NC with a 1 nm height and a 4.7 nm width. The height direction is along [101]. This structure applies to

small CuS NCs such as M11-110 and M11-130. The shape in the lateral dimension is simplified to be quadrangular, but can also be circular or triangular. (C) Large CuS NC with a height of 4.9 nm and a lateral dimension of 20 nm. The height direction is along [001]. This structure applies to large CuS NCs such as M18-90 and M18-130. (D) The morphological evolution of CuS NCs with increasing AS concentration when the Cu(II) concentration is fixed to 1 mM. The facets perpendicular to and parallel to the *c* axis are in dark red and olive, respectively. The starch coatings of CuS NCs in (B), (C), and (D) are not included for clarity. (E) The scheme of a small CuS NC enveloped with a starch coating (light green).

The structures of large CuS NCs are different. The structure shown in Figure 3C is proposed based on the clear lattice planes of (110), $(2\bar{1}0)$ and $(1\bar{2}0)$ on the top view TEM of large CuS NCs (Figure 1D to E) and the periodic lattice space of 1.65 nm in the side view matching the CuS *c* lattice parameter (Figure 1G). The height of the large CuS NCs is evidently larger than that of the small CuS NCs and reaches about 5 nm, which is similar to the CuS nanoplatelets (4 nm in height) synthesized in oleylamine.[10] The proposed structures also accord well with the XRD results. Large CuS NCs are platelets with the *c*-axis perpendicular to the faces. Compared with the small CuS NCs (e.g., M11-130), the peaks of (110) ($2\theta = 48.3°$) of large CuS NCs such as M18-90, M14-130, and M18-130 are considerably sharper (Figure 2A and Figure S9).

The Cu:AS ratio determines the morphologies of CuS NCs. The only difference between M1_0.5-130, M11-130, M14-130, and M18-130 is the Cu:AS ratio, which decreases from 2 to 0.125 (Figure 3D). An excess of AS could lower the nucleation growth kinetics to facilitate the growth of small CuS NCs into large CuS NCs. Similar morphological tuning of CuS nanomaterials by adjusting copper and sulfide precursor ratio has been reported.[10, 23, 29, 46] When small CuS NCs are covered by oleylamine, AS is suggested to reduce the steric barrier to aggregation and slowly merge small CuS NCs into large single crystals at room temperature.[10] The microwave heating employed in the present study accelerates this process, since only for 2 min was necessary to form stable NCs. In addition, by increasing the concentrations of Cu(II) and AS in parallel and fixing the Cu:AS ratio at unity, the properties (size, crystal structure, and UV-vis spectrum) of CuS NCs are similar at concentrations below 4 mM (Figure S3, Figure S9, and Figure S11), indicating the potential for scaleup production. Thus, the total Cu, AS and CuS concentrations have insignificant impact on the size and property of the CuS NCs during the fast reaction process. A moderate synthesis temperature, 110 to 160 °C, is required to obtain uniform, small, and pure CuS NCs. Lower or higher synthesis temperatures lead to impurity incorporation and larger sizes, as confirmed by TEM and XRD results (Figure 1C and Figure S9), and lead to lower OD_{980} as discussed in section 2.2.

The presence of starch coating is crucial for the synthesis, storage, and further applications of the CuS NCs. A model of CuS NCs covered with the starch coating is proposed (Figure 3E). Assuming that the density of the CuS NCs and the starch coating are equivalent to their bulk values, i.e., 4.76 g cm^{-3} for CuS and 1.5 g cm^{-3} for starch,[47] the mass loading of starch can be determined. For example, the mass loading of the starch is calculated to be 58% for M11-130 with 1 nm in height and 4.7 nm in width, covered with a 0.9 nm-thick starch coating as shown in Figure 3E. Considering the size distribution of M11-130 (Figure S2H), this value accords well with the TGA result (64%, Figure S8). The starch coating prevents the aggregation of small CuS NCs both during and after the synthesis. M11-130-0 is thus considerably larger than M11-130 in the lateral dimension, as confirmed by AFM and TEM (Figure 1H, Figure 1I, and Figure S3). The hydrodynamic size of M11-130 in MilliQ water was determined to be 16.3 nm (Figure S12A), which matches the core size determined from TEM with addition of the starch layer and associated water molecules on the surface. The hydrodynamic size of M11-130 increased to 164 nm in 0.9 wt.% NaCl (Figure S12B), indicating a possible aggregation. In contrary to M11-130, M11-130-0 precipitated in solution and was about 204 nm in water and unstable in 0.9 wt.% NaCl (about 1299 nm), confirming the improved stability from the starch coating. The hydrodynamic size of M11-130 in MilliQ water slightly increased to 20.6 nm two days after the synthesis (Figure S12A), indicating a good stability of M11-130 in water. Precipitates were observed for M11-130 in 0.9 wt.% NaCl solution stored at room temperature two days after the synthesis, manifesting that the colloidal stability should be improved for future in vivo studies. Moreover, following storage for 80 h at 4 °C after synthesis, M11-130 remained a homogenous green solution, whereas M11-130-0 turned from a green homogenous solution into dark sediments. The sediments can be returned to a green homogenous suspension after sonication for 30 s (Figure S13A-C). The starch-coated CuS NCs with relatively large lateral size displayed great colloidal stability, i.e., M18-130 remained a homogenous green solution and retained photothermal activity after 25 months storage in aqueous solution at 4 °C (Figure S13D). The CuS NCs with small lateral size such as M11-130 had less than 25 months shelf life. The CuS NCs in physiological saline (0.9% NaCl) displayed slightly lower temperature elevation (31.5 °C) than that in MilliQ water (36.5 °C) in response to laser (Figure S13E). In accordance with this result, the UV-vis of M11-130 in 0.9% NaCl solution showed a small drop at 980 nm wavelength (Figure S13F), which might be due to the absorption of ions or changed dielectric function of the medium. In our cellular experiments in Section 2.3 (CuS NCs in biological media), we did not observe aggregates on the microscopic images for starch-coated NCs. The starch coating also imparts excellent hydrophilicity of the CuS NCs. The abundant hydroxyl groups (-OH) in the starch coating would enable further conjugation with antibodies and peptides for targeted photothermal therapy.

2.2. Photo-absorption and Photothermal Effects of CuS NCs

The wavelength of maximum absorbance (λ_{max}) and the light absorbance at the desired laser wavelength (OD_{980}) of different samples are summarized in Figure 1C, Figure 4A, and Figure S11. CuS NCs synthesized with starch showed a significant NIR absorbance difference from the one without starch (Figure 4B). The λ_{max} of M11-130 was 978 nm, while the broad LSPR of M11-130-0 was shifted to 925 nm and possibly composed of multiple peaks. The OD_{980} of M11-130 was 0.68 corresponding to ~28% higher absorption than that of M11-130-0 (OD_{980} = 0.53). The starch does not have any absorbance in the NIR wavelengths neither before nor after the microwave process (Figure S1). Thus, the starch itself does not show any photothermal effect in response to 980 nm laser illumination (Figure S14). The Cu:AS ratio in the synthesis had a significant impact on the λ_{max} of the CuS NCs in accordance with the observed effect on the NC size (Figure 1C). λ_{max} was 1060 nm for the CuS NCs obtained at a Cu:AS ratio of 2 and 130 °C, but was blueshifted to 978 nm when the ratio was decreased to 1 and then redshifted monotonically to about 1200 nm (outside our observable range) on a further decrease of the ratio to 0.125. A similar trend was observed for the CuS NCs prepared at 90 °C.

The synthesis temperature had only a minor effect on λ_{max} at fixed concentrations and a Cu:AS ratio of 1, fluctuating between 966 and 1017 nm (Figure 1C and Figure S15). Increasing the concentration of Cu(II) and AS in parallel from 0.5 to 10 mM only caused a small variation in λ_{max} ranging from 930 to 978 nm (Figure S3 and Figure S16). All CuS NCs showed significant and comparable OD_{980} except the CuS NCs synthesized at the lowest (70 °C) and the highest temperature (200 °C), or Cu:AS = 2 (**Figure 4**A and Figure S11), for which the OD_{980} was significantly lower. The band gap of CuS NCs was calculated to be 1.4 ~ 2.1 eV (refer to Supplementary Discussion and Figure S17 to Figure S19 for details).

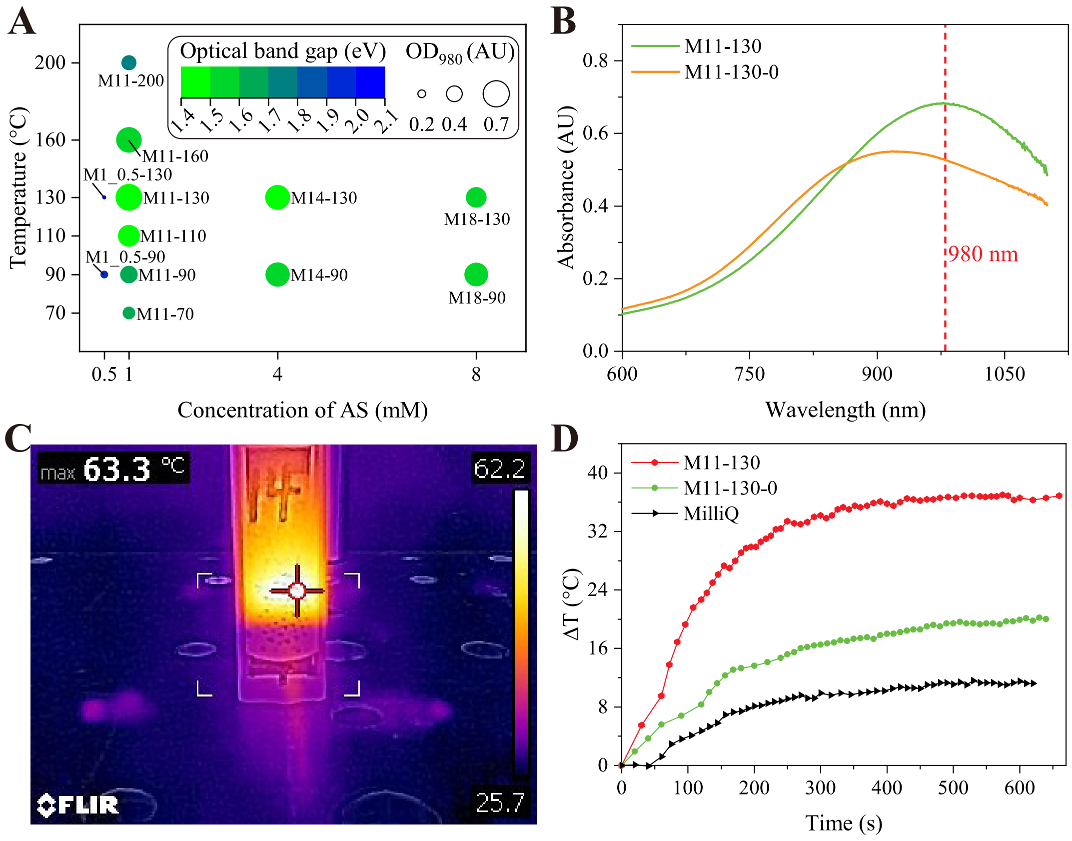

Figure 4. UV-vis spectra and photothermal effect of CuS NCs. (A) Optical band gap and OD_{980} of CuS NCs from different concentrations of AS and synthesis temperature. Details of the UV-vis spectral analysis are presented in Figure S11, Figure S15, and Figure S16. (B) UV-vis spectra of CuS NCs with and without starch. The samples in (A) and (B) were normalized to an initial Cu(II) concentration of 0.2 mM. AU: absorbance units. (C) Thermal imaging of CuS NC dispersions under NIR laser irradiation. CuS NCs in 0.5 mL ultrapure water at 50 mg L^{-1} Cu concentration were prepared in cuvettes. Ultrapure water was used as a control. (D) Temperature curves of CuS NCs synthesized with and without starch. The experiments were conducted at 25 °C.

The photothermal performance of CuS NCs was examined next. The temperature elevation, ΔT, above ambient (i.e., 25 °C) of the CuS NCs dispersions during the LSPR excitation was monitored through a thermal imaging camera (Figure 4C) and plotted against time under a 980 nm-laser illumination at 1.44 W cm^{-2} power density (Figure 4D and Figure S20). The temperature elevations reached the steady state within 10 min at 0.5 mL CuS NCs solutions (50 mg L^{-1} Cu concentration). M11-130 showed a maximum ΔT of 36.9 °C, which is significantly higher than that of M11-130-0 (20.2 °C) and MilliQ water only (11.5 °C) (Figure 4D). The starch coating of CuS NCs thus led to an almost doubling of the temperature elevation. For CuS synthesis using 1 mM Cu(II) and AS, the synthesis temperature had only a modest effect on the maximum ΔT obtained. Similar performance was observed for M11-110 and M11-130, while a slightly smaller maximum ΔT of 34.3 and 28.9 °C were obtained for M11-70 and M11-90, respectively (Figure S20A). The synthesis concentration of Cu(II) and AS had only a slight effect on the maximum Δ*T* which remained in the range 33.3 to 36.9 °C for concentrations from 0.5 to 10 mM, when the synthesis was carried out at 130 °C (Figure S20B). The maximum Δ*T* rose from 28.9 to 35.0 °C as the Cu:AS ratio in the synthesis was decreased from 1:1 to 1:8 at 90 °C (Figure S20C). The gain in the maximum Δ*T* with increasing ratio was small (from 36.9 to 38.6 °C) at the synthesis temperature of 130 °C (Figure S20D). The ambient temperature during photothermal experiments was 25 °C, so the actual temperature of the CuS NCs dispersion was 53.9 to 63.6 °C. Heat treatment between 40 and 45 °C is sufficient to damage cancer cells,[8] indicating that the starch-coated CuS NCs are highly promising as an efficient photothermal therapy agent.

2.3. In Vitro Photothermal Cancer Therapy Efficacy of CuS NCs

The PTT efficacy of CuS NCs was examined on a human prostate cancer cell line PC-3/Luc+ in vitro (**Figure 5**). PC-3/Luc+ cells were treated with various concentrations of CuS NCs with or without 3 minutes 980-nm laser irradiation at 2.48 W cm^{-2} power density. The cell viability was recorded by bioluminescence imaging of the PC-3/Luc+ cells after exposure to D-Luciferin (Figure 5A and B). Live PC-3/Luc+ cells exhibit luminescence on exposure to D-Luciferin, whereas dead PC-3/Luc+ cells do not.[48] A significantly higher photothermal ablation efficiency on the PC-3/Luc+ cells was observed for CuS NCs with starch (M11-130) than for CuS NCs without starch (M11-130-0), as shown in Figure 5C and D. M11-130 at 5 mg L^{-1} Cu concentration with laser irradiation caused 98.4 ± 0.6% death of the cancer cells. This efficiency increased to almost 100% when the concentration increased to 10 and 20 mg L^{-1} (Figure 5C). Bioluminescence signals were barely observed after treatment with M11-130 and laser irradiation (Figure 5A). Conversely, only a 23.7 ± 11.7% cell death was observed after the treatment with 5 mg L^{-1} M11-130-0 and laser. The cell death increased to 64.9 ± 27.1% and 98.4 ± 2.4% when the dose was increased to 10 and 20 mg L^{-1} M11-130-0 with laser, respectively (Figure 5D).

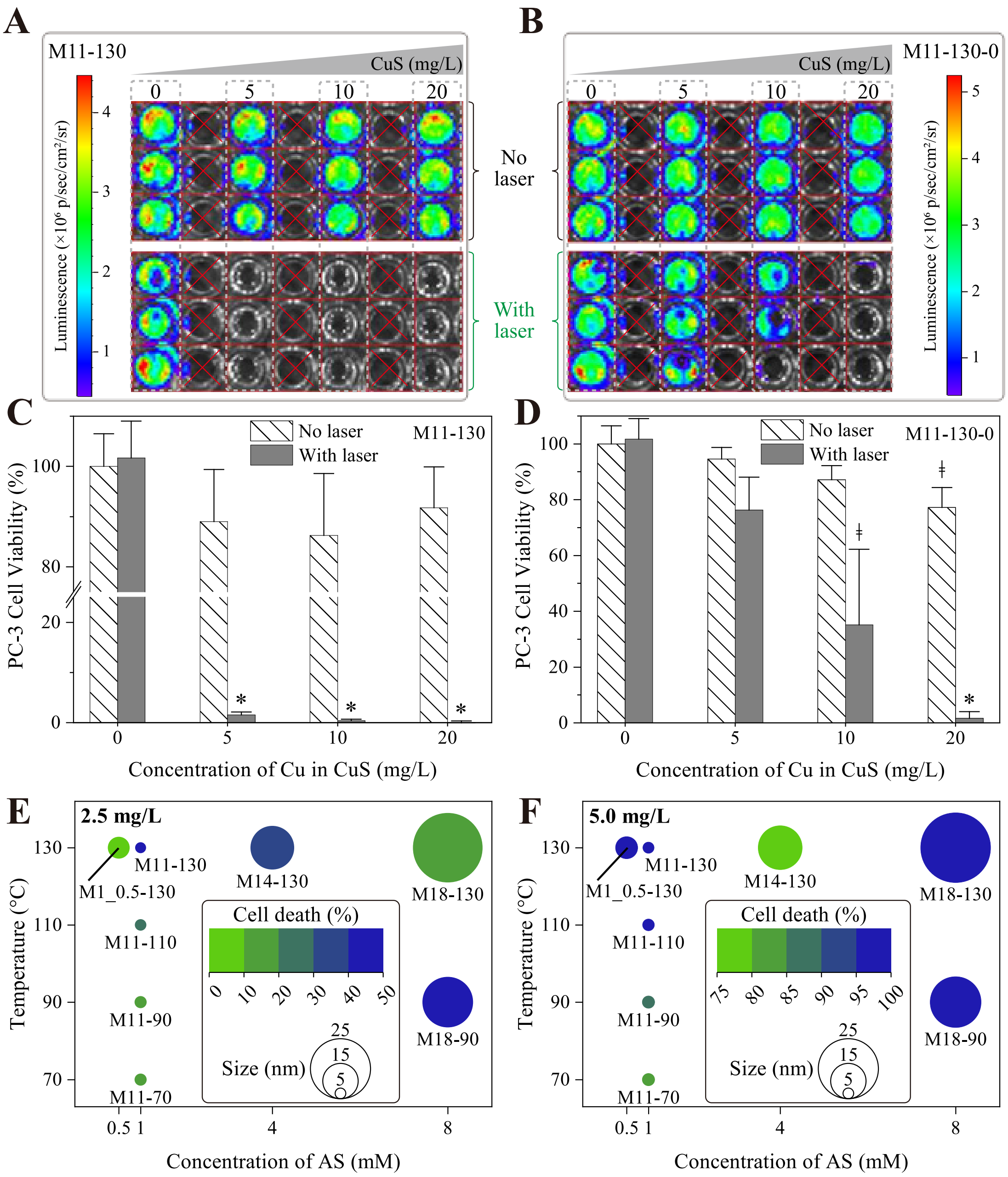

Figure 5. Photothermal ablation of PC-3/Luc+ cancer cells by CuS NCs. In vitro bioluminescence imaging of PC-3/Luc+ cells after photothermal ablation with (A) M11-130 and (B) M11-130-0 as compared to the controls. Top 3 rows: without laser treatment; bottom 3

rows: with laser treatment. The crosses indicate the wells are empty. Cell viability after treatment by (C) M11-130 and (D) M11-130-0 at 0, 5, 10, and 20 mg L^{-1} Cu with and without laser. * $p < 0.0003$, ǂ $p < 0.05$ compared to the control experiments. Comparison of photothermal ablation by different CuS NCs at (E) 2.5 mg L^{-1} and (F) 5.0 mg L^{-1} Cu. The cell death is an average value from three replicates. Note that the scales of cell death are different in (E) and (F). Detailed results of (E) and (F) are presented in Figure S21.

The starch-coated CuS NCs had little cytotoxicity as demonstrated in PC-3/Luc+ cells with up to 50 mg/L concentration of CuS NCs for 24 h treatment. The CuS NCs treated cells showed comparable cell viabilities to that of the control group without CuS NCs ($p > 0.2$, Figure S22). The non-cytotoxicity profile of the starch-coated CuS NCs is also shown in Figure 5A and C (i.e. “no laser”), and Figure S21. For example, M11-130 alone without laser irradiation caused only insignificant decrease in cell viability to 89.0 ± 10.4%, 86.3 ± 12.3%, and 91.8 ± 8.1% with 5, 10, and 20 mg L^{-1} M11-130 ($p = 0.2$ compared to the control cells) respectively (Figure 5C). The cell viability decreased monotonically from 94.6 ± 4.2% ($p = 0.2$ compared to the control cells) to 77.3 ± 7.1% ($p = 0.01$ compared to the control cells) with 5 to 20 mg L^{-1} M11-130-0 without laser treatment, respectively (Figure 5D). Cancer cells without CuS NCs administration treated with laser showed cell viability (101.7 ± 7.4%) comparable to the control cells (100 ± 6.5%). Thus, the laser treatment alone without CuS NCs did not change the cell viability, indicating that the laser power density of 2.48 W cm^{-2} at 980 nm alone had a negligible effect on the cells. Cellular microscopic imaging showed a visible difference in cell morphologies between cancer cells treated with M11-130 and M11-130-0. The number of cancer cells drastically decreased after treatment of M11-130 with laser irradiation. No CuS NC aggregation was observed, indicating that the CuS NCs were well distributed in the medium, or on/in the cancer cells (Figure S23). In contrast, large dark particles were present with the cancer cells after treatment of M11-130-0 either with or without laser irradiation (Figure S24). Aggregation of M11-130-0 is probably partially responsible for the poor performance of this particle type in photothermal ablation.

Further investigations supported that CuS NCs with starch could effectively kill cancer cells with laser irradiation and that the efficiency was related to the synthesis conditions. High synthesis temperature resulted in CuS NCs with high ablation efficiency. M11-130 and M11-110 thus notably outperformed M11-70 and M11-90 at 5.0 and 2.5 mg L^{-1} CuS NCs with laser irradiation (Figure 5E and F, Figure S21). Increasing AS concentration alone during synthesis at 90 °C slightly increased the ablation efficiency. For example, M18-90 was more efficient than M11-90, especially at a dose of 2.5 mg L^{-1} (Figure 5E and F, Figure S21). This trend was not observed for the CuS NCs synthesized at 130 °C. Increasing Cu(II) and AS concentration together during preparation could further improve or maintain the photothermal ablation efficiency. M88-130 thus gave a comparable performance to M11-130, and both were better than M0.5_0.5-130 (Figure S21).

The as-prepared CuS NCs are very efficient photothermal agents. Combined with laser treatment as little as 5 mg L^{-1} CuS can destroy cancer cells effectively, which considerably outperforms reported CuS performances. For example, 11 nm [^{64}Cu]CuS NPs reduced cancer cell densities with a higher NIR laser power (40 W cm^{-2}) for 2 min and at the much higher Cu concentration of 31.78 mg L^{-1}.[49] In another study, about 70% of cancer cell viability was found to be reduced when $Cu_{2-x}S$ nanodots with a Cu concentration of 100 mg L^{-1} and NIR irradiation (1.41 W cm^{-2}, 5 min) were applied.[7] The prodigious photothermal ablation efficacy of the CuS NCs originates from the LSPR photothermal effect rather than other effects such as the potential cytotoxicity from leaking ions since very low cytotoxicity was reported when 3.7 mg L^{-1} copper ions were released from 100 mg L^{-1} Cu_9S_5.[50] In the present study, we used much lower CuS NCs doses (e.g., 5 mg L^{-1}), so potential copper ion leaking is negligible. The photothermal effect of the prepared CuS NCs must therefore be rooted in their particular structure. The preliminary experiments on T47D cells, another widely used human breast cancer cell line,[51] also showed that the CuS NCs are an effective photothermal ablation agent (data not shown), indicating the applicability of the starch-coated CuS NCs photothermal ablation to other cancer cells.

2.4. Modeling of LSPR of CuS NCs

To understand further the relationship between the morphologies of the CuS NCs and their LSPR, we carried out modeling and simulations of the correlation using the finite element method[10, 52] and the program COMSOL Multiphysics with RF solver (COMSOL, Inc., USA). CuS NCs were simplified as nanoplatelets because this shape is dominant. The single layer of starch on CuS NCs was assumed to only affect the structures of CuS NCs and not to be involved in LSPR, and thus was not included in the computational domain for the LSPR simulation of CuS NCs. The typical computational domains therefore included a single CuS NC, two perfectly matched layers absorbing boundary conditions on the top and bottom respectively, a pair of periodic ports (source port below the top perfectly matched layer and listener port above the bottom matched layer), and two pairs of periodic conditions in the *x* and *y* directions, respectively, as shown in Figure S25. The boundary conditions were used to simulate the response of a 2D array of identical CuS NCs with center-to-center *x* and *y* distances as the dimensions of the computer domain in *x* and *y* directions, respectively. A uniform downward-directed plane wave, with **E** field of amplitude $E_x = 2 \times 10^6$ V m^{-1} and parallel to the *x*-axis,[52] was generated by the source port to illuminate the CuS NC. The field satisfies the following equation:

$$\nabla \times (\mu_r^{-1} \nabla \times \mathbf{E}) - k_0^2 \left(\varepsilon_r - j\frac{\sigma}{\omega \varepsilon_0}\right) \mathbf{E} = 0 \tag{1}$$

where μ_r, ε_r, and σ are the relative permeability, the relative permittivity, and the electrical conductivity of the media, respectively. k_0 is the wavenumber in vacuum, *j* the imaginary unit, ω the angular frequency, and ε_0 the permittivity of vacuum (8.8542×10^{-12} m^{-3} kg^{-1} s^4 A^2). For CuS NCs at the NIR frequencies used in this study, $\mu_r = 1$. ε_r depends on frequency and was modeled employing the Drude model:[9, 10, 20, 53-55]

$$\varepsilon_r(\omega) = \varepsilon_\infty - \frac{\omega_p^2}{\omega^2 + i\gamma\omega} \tag{2}$$

where ε_∞ is the background dielectric constant (also called high-frequency dielectric constant), ω_p the Drude plasma frequency, and γ the damping constant (or collision frequency). As a p-type semiconductor, the CuS NC majority carriers are holes. The Drude plasma frequency ω_p is thus related to free carrier (hole) density N_h:[10, 54]

$$\omega_p = \sqrt{\frac{N_h e^2}{m_h \varepsilon_0}} \tag{3}$$

where e is the electron charge (1.6022×10^{-19} C), and m_h the hole effective mass ($0.55\ m_e$, $m_e = 9.109 \times 10^{-31}$ kg).

Values of ε_∞, ω_p, and γ were extracted by fitting extinction spectra of CuS NCs using Gans theory, which describes the LSPR of oblate spheroidal particles distributed randomly in solution:[10, 56]

$$\kappa(\lambda) = \frac{2\pi N V \varepsilon_m^{3/2}}{3\lambda} \sum_{j=A}^{C} \frac{(1/P_j^2)\varepsilon_2}{\left(\varepsilon_1 + \frac{1-P_j}{P_j}\varepsilon_m\right)^2 + \varepsilon_2^2} \tag{4}$$

where $\kappa(\lambda)$ is the absorption coefficient, λ the wavelength, N the number of particles per unit volume, V the volume of the CuS NC, ε_m the permittivity of the ambient medium (here assumed to be non-absorbing water, $\varepsilon_m = 1.33^2 = 1.77$), and ε_1 and ε_2 are the real and imaginary components of ε_r. P_j is the depolarization factor ($j = A, B, and\ C$):

$$P_C = \frac{1+f^2}{f^3}(f - \arctan(f)) \tag{5}$$

$$f = \sqrt{\left(\frac{a}{c}\right)^2 - 1} \tag{6}$$

$$P_A = P_B = \frac{1-P_C}{2} \tag{7}$$

where a and b are the major axes, and c is the minor axis of CuS crystal (a = b > c).

All spectra of the CuS NCs can be fitted with one of the three-parameter sets (ε_∞ and ω_p in **Table 1**). The CuS NCs were thus grouped into three categories: CuS without starch coating, starch-coated CuS NCs with Cu:AS = 1 and M1_0.5-90 as CuS_HCD (high free carrier density), and starch-coated CuS NCs with Cu:AS ≠ 1 except M1_0.5-90 as CuD_LCD (low free carrier density), represented by the ε_∞ and ω_p of M11-130-0, M11-130, and M18-130, respectively, in Table 1. Of note, M1_0.5-90 was categorized as CuS_HCD instead of CuS_LCD, which can be explained by the relatively low synthesis temperature and/or high Cu:AS ratio compared with CuS_LCD and thus the effect of extra precursor was minor.

Table 1. Parameter sets from the fitting of spectra.

Sample	ε_∞	ω_p (rad/s)	γ (1/s)	N_h (cm^{-3})	N
M11-130-0	2.9	3.71×10^{15}	6.63×10^{14}	2.37×10^{21}	1.01×10^{18}
M11-130[a)]	2.7	7.46×10^{15}	7.38×10^{14}	9.63×10^{21}	8.27×10^{17}
M18-130[b)]	7.4	5.43×10^{15}	5.60×10^{14}	5.10×10^{21}	3.32×10^{16}

[a)] The values of ε_∞ and ω_p also show good agreement in the fittings of CuS NCs with high carrier density (CuS_HCD, i.e., starch-coated CuS NCs with Cu:AS = 1 and M1_0.5-90).

[b)] The values of ε_∞ and ω_p also show good agreement in the fittings of CuS NCs with low carrier density (CuS_LCD, i.e., starch-coated CuS NCs with Cu:AS ≠ 1 except M1_0.5-90).

The background dielectric constant (ε_∞) of M11-130-0 is close to that of M11-130, but both are considerably smaller than for M11-180. The value of ε_∞ is related to interband transitions at higher photon energy,[57, 58] implying different interband transitions in M11-130 and M18-130 as well as the difference between CuS_HCD and CuS_LCD. The free carrier density N_h of the CuS NCs was calculated to be of the order of 10^{21} cm^{-3} according with that of similar CuS nanomaterials reported.[11] CuS_HCD has the highest N_h of 9.63×10^{21} cm^{-3}, followed by CuS_LCD with 5.10×10^{21} cm^{-3}, and then CuS without a starch coating with the lowest N_h of 2.37×10^{21} cm^{-3}. The four-fold difference in N_h between CuS NCs with and without starch indicates the key role of starch coating to increase N_h. N_h is also related to the surface states that originate from the defects/inhomogeneities on the surface.[59] The smaller size CuS NCs have a large surface area relative to volume, thus surface states play an important role in determining N_h. It was shown that the surface states trap the holes,[41, 60] and more free carriers are released after the capping process on nanostructures.[59] As such, the starch layer must reduce surface states by introducing surface passivation and thus increases the N_h. As a result, the higher N_h is the main factor for the blueshift of LSPR peak of M11-130 compared to M11-130-0.[10, 60] It was also reported that the formation of $CuSO_4$ can alter the physicochemical properties of the CuS nanomaterials by increasing solubility and ion dissolution, leading to a potential decline in photothermal performance.[39] Moreover, exposure of CuS nanodisks to oxygen was reported to cause blueshift in LSPR.[61] The starch coating in the current study possibly reduces oxygen exposure and ion dissolution. On the other hand, the difference in N_h between CuS_HCD and CuS_LCD is caused by the crystal structural difference.

Different trends of damping constant γ versus the aspect ratio (= height/diameter) were observed within CuS_HCD and CuS_LCD (Figure S26). Damping constants were maintained at a similar level for CuS_HCD but increased with increasing the aspect ratio for CuS_LCD (Figure S26). The damping is caused by the scattering of the electrons with other electrons (charge carriers for semiconductors), lattice defects, phonons, or/and impurities, altogether determining the mean free path of electrons (λ_τ, where the collision time $\tau = 1/\gamma$).[62, 63] For small nanostructures at room temperature, free carriers can be dispersed by the surface of the nanomaterials, termed surface scattering. The observed damping effect implies that surface scattering of free carriers dominates in CuS_LCD,[10, 54, 63] but is unlikely in CuS_HCD. Damping is therefore mainly due to dispersion between the highly dense free carriers in CuS_HCD. All these parameters from the fitting corroborate the different structures of small CuS NCs (typical in CuS_HCD, e.g., M11-130) and large CuS NCs (typical in CuS_LCD, e.g., M18-130) despite that they are all covellite as confirmed by XRD results.

M11-130-0, M11-130, and M18-130, as representatives of CuS NCs without starch coating, CuS_HCD, and CuS_LCD respectively, were further studied to understand the correlation between their structures and plasmon absorption. As CuS NCs are anisotropic LSPR nanostructures, the orientation must be defined, as shown in **Figure 6**A. The in-plane ($\varphi = 90°$ or $\theta = 0°$) and out-of-plane ($\varphi = 0°$, $\theta = 90°$) LSPRs at 600 to 1100 nm of CuS M11-130-0 and M11-130 are shown in Figure 6B and C. Notably, out-of-plane LSPR dominates for M11-130-0 in this wavelength range in contrast to M11-130, which is dominated by in-plane LSPR as reported for CuS nanoplatelets in many previous studies.[10, 23, 54, 64] The out-of-plane LSPR peak of M11-130-0 appears at 916 nm, while that of M11-130 blueshifts to 728 nm. To ascertain the full LSPR of M11-130-0 and M18-130, the wavelength range of simulation is extended (Figure S27). The out-of-plane LSPR peak of M18-130 appears at 1004 nm. In addition, the in-plane LSPR of M11-130-0, M11-130, and M18-130 appears at 2679, 969, and 1592 nm, respectively. Of note, the in-plane LSPR dominates in the full LSPR range for all three CuS NCs (Figure S27). These anisotropic CuS NCs thus have a major in-plane mode at low energy and a minor out-of-plane mode at high energy. CuS_HCD such as M11-130 shifts both modes to higher energy so that the in-plane mode matches the laser wavelength at 980 nm. Simulations of the **E** field intensity and heat power volume density Q_d under a plane wave illumination of 980 nm are detailed for M11-130-0 and M11-130 with in-plane mode and out-of-plane mode in Figure 6D and F. M11-130 apparently shows several times stronger interaction with the **E** field compared to M11-130-0 at 980 nm. Moreover, M11-130 exhibits two orders of magnitude higher Q_d concentrated around the center with in-plane LSPR than its out-of-plane mode as well as that of the M11-130-0 LSPR, whilst Q_d distributes more towards the peripheral in the M11-130-0 NC. The simulation results ascertain that the strong LSPR absorption of M11-130 at 980 nm is attributed to its major in-plane mode with multiply boosted energy at the center of the NC owing to the high free carrier density.

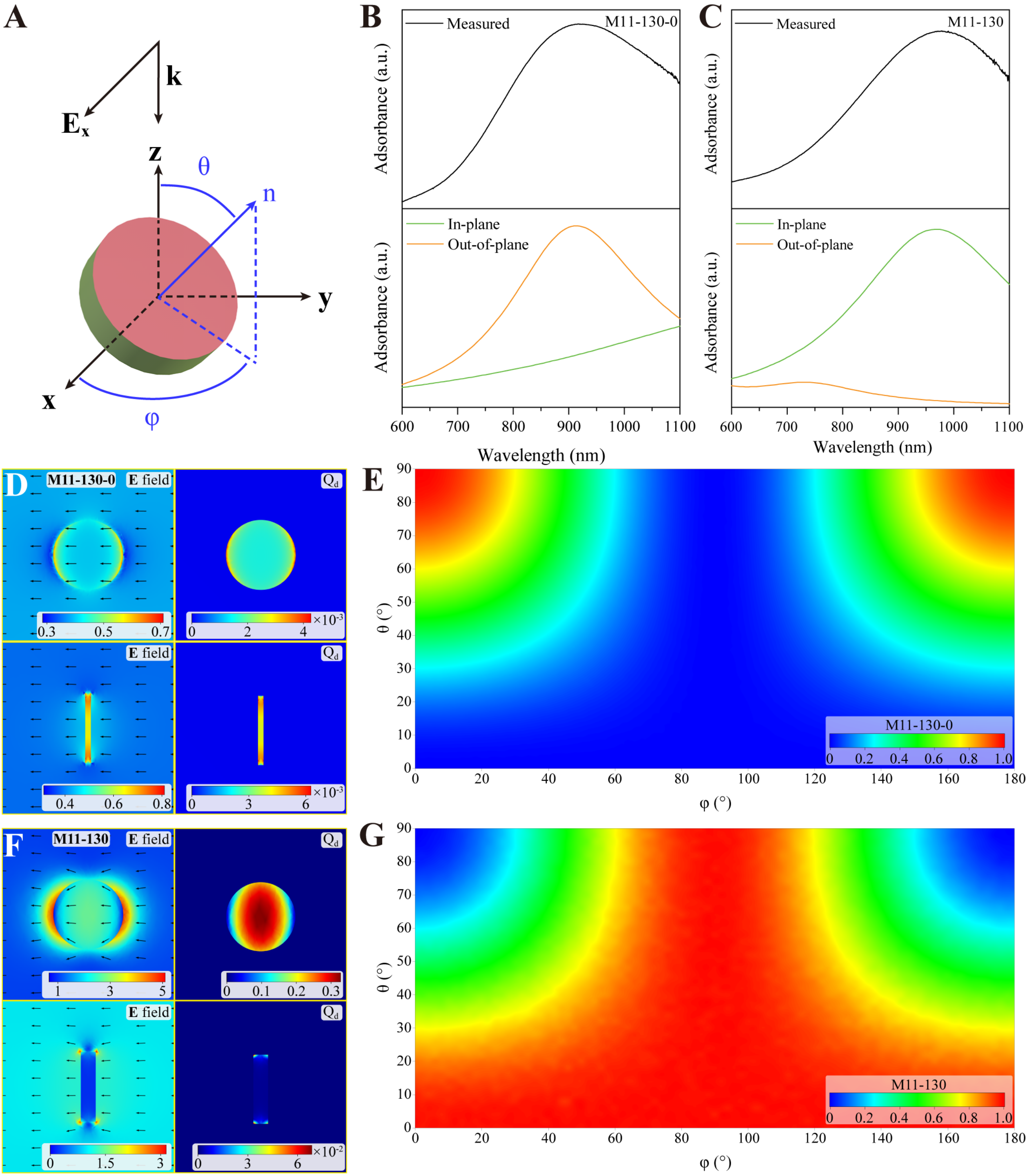

Figure 6. CuS NC plasmonic analysis and simulation. (A) The orientation of CuS NCs, defined by θ, the angle between **n** (axis of rotation) and the *z*-axis, and φ, the angle between the projection of **n** and *x*-axis in the *x*-*y* plane. φ is defined by the rotation along **n** when θ = 0 or 180°. Experimental and simulated spectra of (B) M11-130-0 and (C) M11-130. "a.u." indicates

“arbitrary unit”. **E** field intensity (in V nm^{-1}) and heat power volume density Q_d (in mW nm^{-3}) under a plane wave illumination of 980 nm for (D) M11-130-0 and (F) M11-130 with in-plane mode (upper row) and out-of-plane mode (lower row). The black arrows indicate polarization directions. The effect of particle orientation (θ and φ) on the normalized absorption at 980 nm of (E) M11-130-0 and (G) M11-130, respectively.

The normalized absorption of M11-130-0, M11-130, and M18-130 at 980 nm over the full range of orientations (θ: 0 to 90°, and φ: 0 to 180°) was studied to evaluate their photothermal efficiency as a function of orientation. M11-130-0 gives low absorption at most orientations except those around out-of-plane LSPR (Figure 6E). In contrast, M11-130 absorbs much more strongly over a wide range of orientations (Figure 6G). The absorption of M11-130 and M11-130-0 at each orientation was further compared. Strikingly, absorption of M11-130 at 96% of orientations is higher than that of M11-130-0, especially around in-plane LSPR, which is higher by 34.7 times (Figure S28). This is because orientation-dependent surface scattering dominates LSPR for M11-130-0 with much smaller N_h. However, the damping in M11-130 is dominated by the internal scattering (i.e., holes with other holes, lattice defects, *etc.*) which is less dependent on the orientation. M18-130 exhibits similar trends as M11-130 (Figure S29). To compare the absolute absorption of the CuS NCs at 980 nm, the absorption cross-section over the full range of orientations is presented (Figure S30). Statistically, the mean absorption cross-section is estimated to be 5.1×10^{-13} m^2, 2.8×10^{-13} m^2, and 0.4×10^{-13} m^2 for M11-130, M18-130, and M11-130-0, respectively. In solution conditions, M11-130 and M18-130 therefore have the same order of magnitude and comparable absorptions, whilst the mean absorption of

M11-130-0 is an order of magnitude lower. This is consistent with the experimental extinction spectra and the equivalent photothermal performance of M11-130 and M18-130 at 980 nm (Figure S20D), as well as with the poor photothermal performance of M11-130-0 (Figure 4D) that we observed.

3. Conclusion

We have developed a rapid, straightforward, and environmentally friendly chemical synthesis of starch-coated CuS NCs which exhibited a high in vitro photothermal ablation efficacy in human prostate cancer PC-3/Luc+ cells. The single-layer starch coating imparts excellent aqueous dispersibility on the CuS NCs, reduces and homogenizes the size of the CuS NCs. The decisive factor in the morphological regulation is the ratio of Cu:AS. Small CuS NCs are obtained with the ratio of Cu:AS = 1, while large CuS NCs are obtained with the ratio < 1. Further multifarious characterizations revealed differences in heights and crystal structures between small and large CuS NCs, leading to red-shifted LSPR of large CuS NCs compared to small CuS NCs.

Very notably, starch-coated CuS NCs such as M11-130 and M18-130 achieved as high as 98.4% cancer cell death with a dose as low as 5 mg L^{-1} and 980 nm laser illumination (2.48 W cm^{-2}) for 3 min. Plasmonic analysis and simulation disclose that the physical origin of the starch coating enhances the photothermal performance by increasing the free carrier density and thus decreasing the mean free path of carriers. In turn, this alters the dominant LSPR mode from out-of-plane to in-plane and shifts the majority orientations from low absorption to high absorption at 980 nm. When the size of coated CuS NCs increases, the free carrier density decreases, and both in-plane and out-of-plane LSPR modes are red-shifted. Consequently, as the laser frequency now lies between the two LSPR mode frequencies, the absorption range for different orientations is narrowed around the mean level of small starch-coated CuS NCs. Parallel photothermal performance and in vitro photothermal ablation is thus maintained at 980 nm.

Collectively, both our experimental investigations and theoretical modeling support the conclusion that starch-coated CuS NCs are photothermally highly efficient ultrasmall nanocrystals, the morphology and LSPR absorption of which can be controlled precisely. CuS NCs with different morphologies can behave differently in biological tissue, and thus the in vivo photothermal ablation is the focus of our forthcoming research. Overall, the study provides a unified outcome of design, simple chemical synthesis, characterization, LSPR modeling, and application, with notable outcomes of photothermally and cytotoxically highly efficient CuS NCs and the basis for exciting in vivo and other new studies of the new nanomaterials. Such atomically thin small CuS NCs with excellent photothermal efficiency, good water dispersibility, and biocompatibility show great potential for clinical translation in photothermal therapy of cancers.

4. Experimental Section

Reagents. $CuCl_2 \cdot 2H_2O$ (Analytical Reagent) was from Riedel-de Haën, France, ammonium sulfide (20 wt.% in H_2O), hydrochloric acid (ACS reagent, 37%), and soluble starch (from potato, acc. to Zulkowsky) from Sigma-Aldrich, Germany. Nitric acid (70%) was from Fisher chemical, UK, RPMI-1640 medium and other cell culture reagents from Fisher Scientific or

Sigma-Aldrich (St. Louis, Missouri, USA). Heat-inactivated fetal bovine serum (FBS) was from Hyclone Laboratories, Logan, UT, USA, and D-luciferin from Promega, Madison, Wisconsin, USA. All chemicals were used without further purification. Ultrapure water or MilliQ water (18.2 MΩ cm) was obtained from a Sartorius Arium Pro system or a Millipore Synergy Remote UV Purification system, was used throughout.

Synthesis of CuS nanocrystals. In a typical synthesis, starch (0.030 g) was dissolved in ultrapure water (15 mL). $CuCl_2 \cdot 2H_2O$ solution (15 µL, 1 M) was added to the starch solution, forming a transparent pale blue solution. Ammonium sulfide (AS) was added to the solution to a final concentration of 1 mM, turning the color of the solution brown. After 5 min, the reaction mixture was heated to 130 °C for 2 min by a microwave synthesizer (Biotage Initiator), turning the solution green. Stirring was maintained during the entire synthesis, including microwave heating. The mixture was then transferred to ice-cold water to cool down and dialyzed with ultrapure water for 48 h in a dialysis tubing cellulose membrane (typical molecular mass cut-off = 14000 Amu, Sigma-Aldrich, Germany). The CuS NC suspensions were stored at 4 °C. The products are denoted as "MXY-Z", where "M" indicates microwave synthesis, while "X" and "Y" indicate the copper chloride and AS concentrations in mM and "Z" the synthesis temperature in °C. A suffix of "-0" is added to the product M11-130-0, where starch was omitted from the synthesis.

Characterization. TEM samples were cast on ultrathin carbon-coated copper grids (Ted Pella Inc., Redding CA, USA) by placing one drop of sample dispersion onto the grid. The samples were imaged using a Tecnai G2 T20 instrument (FEI Company, Hillsboro, USA). One drop (4

~ 10 μL) of sample dispersion was placed on a freshly cleaved mica sheet and dried in air at ambient temperature overnight for AFM. AFM was recorded using an Agilent 5500 SPM (Agilent Technologies, Chandler, AZ, USA) equipped with an Arrow NCR probe (NanoWorld, Switzerland) in tapping mode in air under ambient conditions. For XPS, sample dispersion (about 5 μL) was cast on a silicon wafer and data recorded using a Thermo Scientific K-alpha spectrometer with Al K_α radiation. Absorption spectra of CuS NCs were recorded using an Agilent 8453 UV-vis spectrophotometer (Santa Clara, USA) with a 1 cm light path quartz cuvette. XRD data were recorded using a Huber (Rimsting, Germany) G670 Guinier imaging plate camera and Cu K_α radiation with freeze-dried samples. TGA was carried out using a TGA/DSC STAR^e System (Mettler Toledo) measured in N_2 with a ramping rate of 5 °C min^{-1} from room temperature to 700 °C. Copper concentration in the samples was quantified using inductively coupled plasma-optical emission spectrometry (Thermo scientific; iCAP 7000 series) after dissolution in aqua regia (mixture of 70% HNO_3 and 37% HCl with a volume ratio of 1:3). Hydrodynamic size distrubustions of CuS NCs were characterized by dynamic light scattering using a Malvern ZetaSizer Nano ZS (Malvern Instruments, Worcestershire, UK). The measurements were conducted on 1 mL sample with a backscattering angle of 173° and three replicates.

Photothermal effect in aqueous solution. A continuous-wave fiber-coupled NIR laser (CivilLaser LSR980H-FC-8W, NaKu Technology Co. Ltd., China) with a center wavelength of 980 nm was used for the photothermal experiments. The laser was coupled to a three-meter, 400 μm core high power optical fiber with an SMA connector at the output to deliver the laser beam from the laser source to the target. The fiber output was fixed on an SMA adaptor and a N-BK7 uncoated plano-convex lens mounted at the fiber output. The fiber output tip was positioned slightly off the focal point of the lens to collimate the laser beam with a small divergence angle. Hence the laser beam diameter at the target can be adjusted by changing the distance between the target and the lens. The laser power at the target was calibrated and measured using a photodiode sensor 918D and an optical power meter 1918 (Newport Co., USA). To determine the photothermal effect mediated by CuS NCs, the fiber-lens assembly was mounted 5 cm above the sample cell using an adjustable stage. The laser output power was 1.5 W. The power density was calculated to be 1.44 W cm^{-2} at the target surface. The laser beam was delivered above the solution containing CuS NCs (0.5 mL) in a 10 mm × 10 mm plastic cuvette. An infrared thermal imaging camera (FLIR C3, FLIR Systems Inc., USA) was used to monitor the temperature of the CuS NCs dispersion. Ultrapure water was used as a control.

Photothermal ablation of cancer cells. The stable luciferase-expressing PC-3/Luc+ cells were prepared as described and kept by the Cell and Immunobiology Core Facility at the University of Missouri-Columbia, USA.[48] PC-3/Luc+ cells were seeded on a 96-well plate at a density of 2×10^4 cells (100 μL) per well in RPMI-1640 medium (containing 10% fetal bovine serum (FBS) and 1% antibiotics) and incubated in a humidified incubator at 37 °C in the presence of 5% CO_2 for 24 h before treatment. The medium was then aspirated from the cell plate. CuS NCs dispersed in RPMI-1640 culture medium (100 μL) were added to each well at different copper ion concentrations. Medium without CuS NCs was used as a control. After 2 h of incubation, each well was irradiated by a fiber-coupled diode NIR laser centered at 980 nm at an output power of 1.5 W with an effective power density calculated to be 2.48 W cm^{-2} at the target well for 3 min. After treatment, the culture medium was aspirated, and 100 µL RPMI-1640 medium added to each well. The cells were incubated for 24 h at 37 °C in 5% CO_2, then exposed to D-Luciferin to exhibit luminescence, and the plates imaged for live cell counting. Briefly, 100 µL D-luciferin (150 mg L^{-1}) was added to each well and incubated for five minutes to activate the luciferase PC-3/Luc+ cells. After aspiration of the media from the cultured cells, bioluminescence imaging was immediately recorded to detect the live cells using an in vivo imaging system IVIS Spectrum (Perkin Elmer, USA). The cell morphologies in each well were visualized under a HAL-100 microscope (Zeiss, USA).

Cytotoxicity of CuS NCs. PC-3/Luc+ cells were seeded on a 96-well plate in media and incubated for 24 h at 37 °C in the presence of 5% CO_2. The media was replaced with fresh media containing different concentrations of CuS NCs, and the cells were incubated for 24 h at 37 °C in the presence of 5% CO_2. After the incubation, the cells were exposed to D-luciferin, and the bioluminescence imaging for cell viability assay (detailed above) was performed.

Statistical Analysis. Data are presented as mean ± standard deviation. Comparisons of in vitro experimental and control groups were performed using Student's *t* test. Significance is defined with P values less than 0.05.

Supporting Information

Supporting Information is available from the Wiley Online Library or the authors.

Acknowledgments

This work was partially supported by China Scholarship Council (No.201606130019), Danish Agency for Science, Technology and Innovation International Network Programme (No. 6144-00069B), the Otto Mønsted foundation, Lundbeckfonden Visiting Professorship (No. R290-2018-1021), and University of Missouri School of Medicine Bridge Funding. We acknowledge the support and resources provided by the Harry S. Truman Veterans Memorial Hospital in Columbia, MO, USA.

Conflict of Interest

The authors declare no conflict of interest.

References

[1] A. R. Makkouk, S. J. Madsen, *Nanoparticle-mediated photothermal therapy of brain tumors*, Springer New York, NY, USA **2013**.

[2] J. Beik, Z. Abed, F. S. Ghoreishi, S. Hosseini-Nami, S. Mehrzadi, A. Shakeri-Zadeh, S. K. Kamrava, *J. Controlled Release* **2016**, *235*, 205.

[3] B. Schwartzberg, J. Lewin, O. Abdelatif, J. Bernard, H. Bu-Ali, S. Cawthorn, M. Chen-Seetoo, S. Feldman, S. Govindarajulu, L. Jones, A. Juette, S. Kavia, R. Maganini, S. Pain, M. Shere, C. Shriver, S. Smith, A. Valencia, E. Whitacre, R. Whitney, *Ann. Surg. Oncol.* **2018**, *25*, 2958.

[4] S. Natarajan, S. Raman, A. M. Priester, J. Garritano, D. J. A. Margolis, P. Lieu, M. L. Macairan, J. Huang, W. Grundfest, L. S. Marks, *J. Urol.* **2016**, *196*, 68.

[5] A. R. Rastinehad, H. Anastos, E. Wajswol, J. S. Winoker, J. P. Sfakianos, S. K. Doppalapudi, M. R. Carrick, C. J. Knauer, B. Taouli, S. C. Lewis, A. K. Tewari, J. A. Schwartz, S. E. Canfield, A. K. George, J. L. West, N. J. Halas, *Proc. Natl. Acad. Sci. U. S. A.* **2019**, *116*, 18590.

[6] X. Li, J. F. Lovell, J. Yoon, X. Chen, *Nat. Rev. Clin. Oncol.* **2020**, *17*, 657.

[7] J. Mou, P. Li, C. Liu, H. Xu, L. Song, J. Wang, K. Zhang, Y. Chen, J. Shi, H. Chen, *Small* **2015**, *11*, 2275.

[8] Q. Tian, M. Tang, Y. Sun, R. Zou, Z. Chen, M. Zhu, S. Yang, J. Wang, J. Wang, J. Hu, *Adv. Mater.* **2011**, *23*, 3542.

[9] Y. Liu, M. Liu, M. T. Swihart, *J. Phys. Chem. C* **2017**, *121*, 13435.

[10] M. Liu, X. Xue, C. Ghosh, X. Liu, Y. Liu, E. P. Furlani, M. T. Swihart, P. N. Prasad, *Chem. Mater.* **2015**, *27*, 2584.

[11] C. Coughlan, M. Ibáñez, O. Dobrozhan, A. Singh, A. Cabot, K. M. Ryan, *Chem. Rev.* **2017**, *117*, 5865.

[12] X.-Y. Zhang, D. Han, N. Ma, R. Gao, A. Zhu, S. Guo, Y. Zhang, Y. Wang, J. Yang, L. Chen, *J. Phys. Chem. Lett.* **2018**, *9*, 6047.

[13] H. Chen, L. Shao, Q. Li, J. Wang, *Chem. Soc. Rev.* **2013**, *42*, 2679.

[14] J. B. Vines, J.-H. Yoon, N.-E. Ryu, D.-J. Lim, H. Park, *Front. Chem.* **2019**, *7*.

[15] N. S. Abadeer, C. J. Murphy, *J. Phys. Chem. C* **2016**, *120*, 4691.

[16] L. R. Hirsch, R. J. Stafford, J. A. Bankson, S. R. Sershen, B. Rivera, R. E. Price, J. D. Hazle, N. J. Halas, J. L. West, *Proc. Natl. Acad. Sci. U. S. A.* **2003**, *100*, 13549.

[17] M. J. Mitchell, M. M. Billingsley, R. M. Haley, M. E. Wechsler, N. A. Peppas, R. Langer, *Nat. Rev. Drug Discovery* **2021**, *20*, 101.

[18] A. K. Iyer, G. Khaled, J. Fang, H. Maeda, *Drug Discov. Today* **2006**, *11*, 812.

[19] S. Sun, P. Li, S. Liang, Z. Yang, *Nanoscale* **2017**, *9*, 11357.

[20] J. M. Luther, P. K. Jain, T. Ewers, A. P. Alivisatos, *Nat. Mater.* **2011**, *10*, 361.

[21] X. Liu, M. T. Swihart, *Chem. Soc. Rev.* **2014**, *43*, 3908.

[22] A. Morales-García, A. L. Soares, E. C. Dos Santos, H. A. de Abreu, H. A. Duarte, *J. Phys. Chem. A* **2014**, *118*, 5823.

[23] R. Lesyuk, E. Klein, I. Yaremchuk, C. Klinke, *Nanoscale* **2018**, *10*, 20640.

[24] C. N. R. Rao, H. S. S. Ramakrishna Matte, U. Maitra, *Angew. Chem. Int. Ed.* **2013**, *52*, 13162.

[25] W. Feng, W. Nie, Y. Cheng, X. Zhou, L. Chen, K. Qiu, Z. Chen, M. Zhu, C. He, *Nanomedicine* **2015**, *11*, 901.

[26] L. Guo, I. Panderi, D. D. Yan, K. Szulak, Y. Li, Y.-T. Chen, H. Ma, D. B. Niesen, N. Seeram, A. Ahmed, B. Yan, D. Pantazatos, W. Lu, *ACS Nano* **2013**, *7*, 8780.

[27] K. Zulkowsky, *Ber. Dtsch. Chem. Ges.* **1880**, *13*, 1395.

[28] K. Zulkowski, *Ber. Dtsch. Chem. Ges.* **1890**, *23*, 3295.

[29] Z. Yang, Z. Wu, J. Liu, Y. Liu, S. Gao, J. Wang, Y. Xiao, Y. Zhong, B. Zhong, X. Guo, *J. Mater. Chem. A* **2020**, *8*, 8049.

[30] T. Heitmann, E. Wenzig, A. Mersmann, *Enzyme Microb. Technol.* **1997**, *20*, 259.

[31] Y. Du, Z. Yin, J. Zhu, X. Huang, X.-J. Wu, Z. Zeng, Q. Yan, H. Zhang, *Nat. Commun.* **2012**, *3*, 1177.

[32] H. Cao, Z. Zheng, J. Meng, X. Xiao, P. Norby, S. Mossin, *Electrochim. Acta* **2020**, *356*, 136791.

[33] Y. Fan, Y. Li, X. Han, X. Wu, L. Zhang, Q. Wang, *Molecules* **2019**, *24*, 3776.

[34] A. V. Bulgakova, D. S. Sofronov, P. V. Mateichenko, V. N. Baumer, A. A. Beda, V. A. Chebanov, *Prot. Met. Phys. Chem. Surf.* **2016**, *52*, 448.

[35] Q. Chen, Y. Yao, X. Li, J. Lu, J. Zhou, Z. Huang, *J. Water Process. Eng.* **2018**, *26*, 289.

[36] A. Aracena, F. Fernández, O. Jerez, A. Jaques, *Hydrometallurgy* **2019**, *188*, 31.

[37] C. M. Simonescu, V. S. Teodorescu, O. Carp, L. Patron, C. Capatina, *J. Therm. Anal. Calorim.* **2007**, *88*, 71.

[38] L. Isac, I. Popovici, A. Enesca, A. Duta, *Environ. Eng. Manage. J.* **2011**, *10*.

[39] H. Wu, V. W. Or, S. Gonzalez-Calzada, V. H. Grassian, *Nanoscale* **2020**, *12*, 19350.

[40] H. Evans, J. Konnert, *Am. Mineral.* **1976**, *61*, 996.

[41] J. Ludwig, L. An, B. Pattengale, Q. Kong, X. Zhang, P. Xi, J. Huang, *J. Phys. Chem. Lett.* **2015**, *6*, 2671.

[42] Q.-L. Li, Y. Sun, L. Ren, X. Wang, C. Wang, L. Li, Y.-W. Yang, X. Yu, J. Yu, *ACS Appl. Mater. Interfaces* **2018**, *10*, 29314.

[43] M. Ye, X. Wen, N. Zhang, W. Guo, X. Liu, C. Lin, *J. Mater. Chem. A* **2015**, *3*, 9595.

[44] S. Radhakrishnan, H.-Y. Kim, B.-S. Kim, *Sens. Actuators, B* **2016**, *233*, 93.

[45] W. Fu, M. Liu, F. Xue, X. Wang, Z. Diao, L. Guo, *RSC Adv.* **2016**, *6*, 80361.

[46] J. Luo, N. Yu, Z. Xiao, C. Long, D. K. Macharia, W. Xu, L. Zhang, M. Zhu, Z. Chen, *J. Alloys Compd.* **2015**, *648*, 98.

[47] C. Engelbrekt, K. H. Sørensen, T. Lübcke, J. Zhang, Q. Li, C. Pan, N. J. Bjerrum, J. Ulstrup, *ChemPhysChem* **2010**, *11*, 2844.

[48] Q.-Y. Cai, P. Yu, C. Besch-Williford, C. J. Smith, G. L. Sieckman, T. J. Hoffman, L. Ma, *Prostate* **2013**, *73*, 842.

[49] M. Zhou, R. Zhang, M. Huang, W. Lu, S. Song, M. P. Melancon, M. Tian, D. Liang, C. Li, *J. Am. Chem. Soc.* **2010**, *132*, 15351.

[50] Q. Tian, F. Jiang, R. Zou, Q. Liu, Z. Chen, M. Zhu, S. Yang, J. Wang, J. Wang, J. Hu, *ACS Nano* **2011**, *5*, 9761.

[51] A. F. Prasanphanich, L. Retzloff, S. R. Lane, P. K. Nanda, G. L. Sieckman, T. L. Rold, L. Ma, S. D. Figueroa, S. V. Sublett, T. J. Hoffman, C. J. Smith, *Nucl. Med. Biol.* **2009**, *36*, 171.

[52] F. Alali, I. H. Karampelas, Y. H. Kim, E. P. Furlani, *J. Phys. Chem. C* **2013**, *117*, 20178.

[53] S.-W. Hsu, K. On, A. R. Tao, *J. Am. Chem. Soc.* **2011**, *133*, 19072.

[54] Y. Xie, L. Carbone, C. Nobile, V. Grillo, S. D'Agostino, F. Della Sala, C. Giannini, D. Altamura, C. Oelsner, C. Kryschi, P. D. Cozzoli, *ACS Nano* **2013**, *7*, 7352.

[55] N. W. Ashcroft, N. D. Mermin, *Solid state physics*, Cengage Learning, **1976**.

[56] S. Link, M. B. Mohamed, M. A. El-Sayed, *J. Phys. Chem. B* **1999**, *103*, 3073.

[57] F. Vischio, E. Fanizza, V. De Bellis, T. Sibillano, C. Ingrosso, C. Giannini, V. Laquintana, N. Denora, A. Agostiano, M. Striccoli, M. L. Curri, N. Depalo, *J. Phys. Chem. C* **2019**, *123*, 23205.

[58] F. Scotognella, G. Della Valle, A. R. Srimath Kandada, D. Dorfs, M. Zavelani-Rossi, M. Conforti, K. Miszta, A. Comin, K. Korobchevskaya, G. Lanzani, L. Manna, F. Tassone, *Nano Lett.* **2011**, *11*, 4711.

[59] N. V. Hullavarad, S. S. Hullavarad, *J. Vac. Sci. Technol., A* **2008**, *26*, 1050.

[60] Z. Lian, M. Sakamoto, H. Matsunaga, J. J. M. Vequizo, A. Yamakata, M. Haruta, H. Kurata, W. Ota, T. Sato, T. Teranishi, *Nat. Commun.* **2018**, *9*, 2314.

[61] T. Wei, Y. Liu, W. Dong, Y. Zhang, C. Huang, Y. Sun, X. Chen, N. Dai, *ACS Appl. Mater. Interfaces* **2013**, *5*, 10473.

[62] E. A. Coronado, G. C. Schatz, *J. Chem. Phys.* **2003**, *119*, 3926.

[63] C. Noguez, *J. Phys. Chem. C* **2007**, *111*, 3806.

[64] R. Zhao, X. Sun, J. Sun, L. Wang, J. Han, *RSC Adv.* **2017**, *7*, 10143.

Supporting Information

Starch Capped Atomically Thin CuS Nanocrystals for Efficient Photothermal Therapy

Zhiyong Zheng, Ping Yu, Huili Cao, Mengyu Cheng, Thomas Zhou, Li E. Lee, Jens Ulstrup, Jingdong Zhang, Christian Engelbrekt, and Lixin Ma**

Contents

Supplementary Discussion

Determination of band gap of CuS NCs.

The optical band gap (E_g, eV) of the CuS NCs was calculated through Tauc's equation:[1-4]

$$\alpha h v = C_a \left(h v - E_g\right)^n \tag{S1}$$

where α is the absorption coefficient, h Planck's constant, v the frequency, C_α an optical transition dependent constant of the material, and n a number relating to the mechanism of electronic transition. As an indirect allowed transition, $n = 2$ for CuS NCs [3]. α can be calculated according to Beer–Lambert's law:[2, 5]

$$\alpha = \frac{A ln 10}{d} \tag{S2}$$

where A is the absorbance and d the light path length. Since scattering is negligible for these samples (Figure S17), we recorded absorbance was measured directly from transmission-based UV-vis spectra. Then Tauc plot was obtained, which shows light energy (hv) on the x-axis and quantity $(\alpha \mathrm{hv})^{1/n}$ on the y-axis. The linear regime of the Tauc plot indicates the onset of absorption. E_g can be determined by extrapolating the linear regime of the $(\alpha hv)^{1/2}$ versus hv to $\alpha = 0$, as shown in Figure S18 and Figure S19. The values of E_g are summarized in Figure 3A and Figure S11. E_g of CuS NCs obtained with Cu:AS ratio of 0.5 (1.9 and 2.1 eV at 90 and 130 °C respectively) were considerably higher than CuS NCs with other ratios, which were in the range 1.4 to 1.6 eV at 90 and 130 °C. The E_g was smallest at an intermediate temperature of 130 °C (1.4 eV) and increased to 1.7 eV when the temperature was either decreased to 70 °C or increased to 200 °C (Figure 3A). E_g varied insignificantly between 1.4 to 1.7 eV when the concentration of Cu and AS was increased from 0.5 to 10 mM (Figure S11).

Supporting Figures and Tables

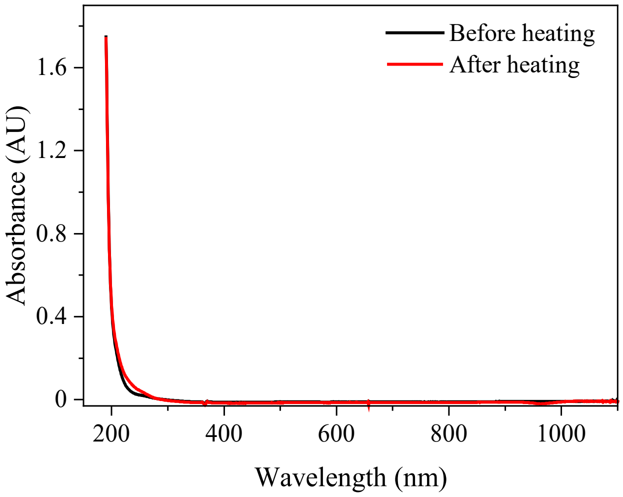

Figure S1. UV-vis spectra of starch before and after microwave heating (at the same starch concentration corresponding to 1 mM Cu(II) in the synthesis) at 130 °C, 2 min. Starch shows no absorbance in the NIR wavelength range.

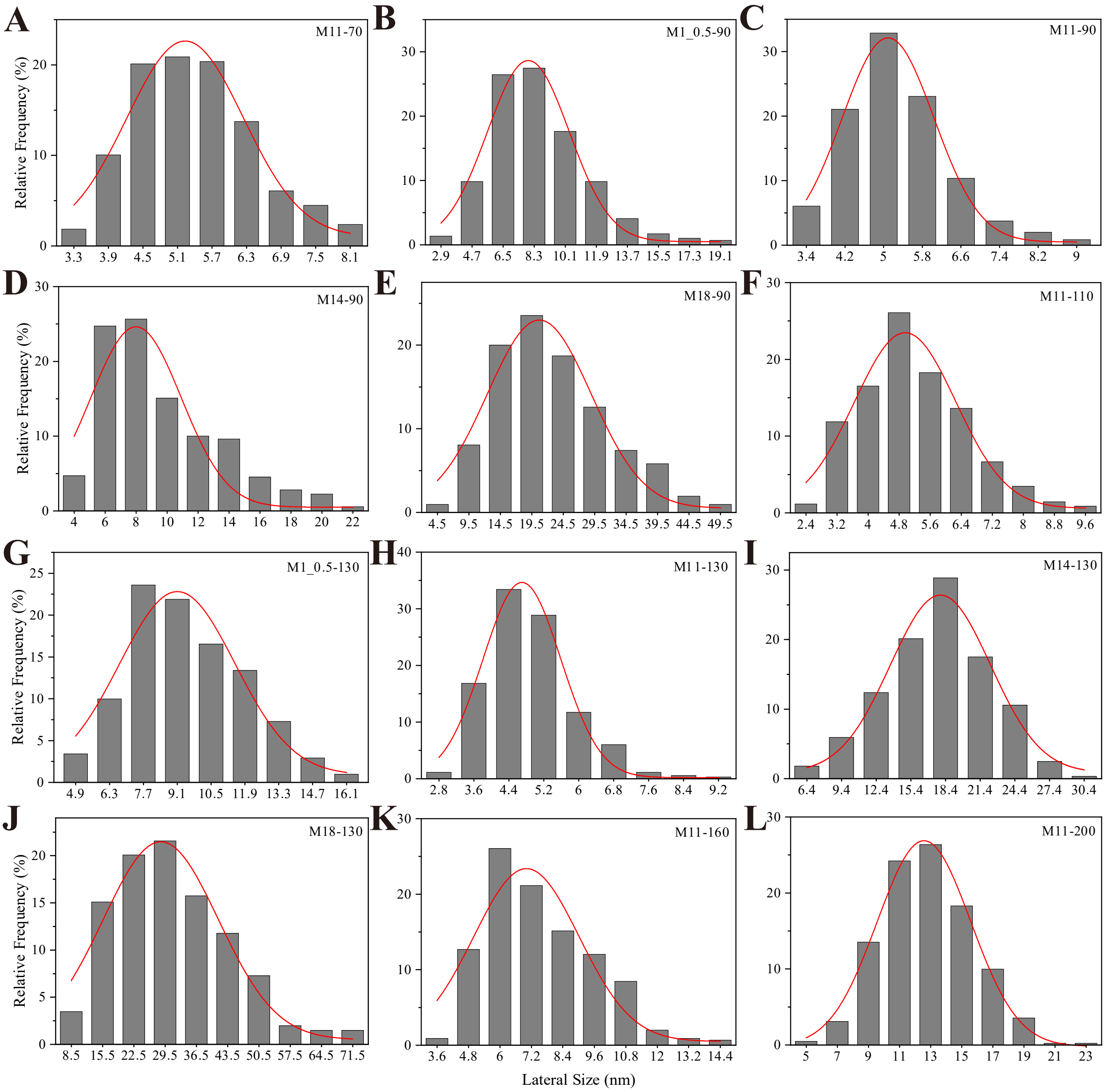

Figure S2. Size distribution of CuS NCs synthesized with different concentrations of AS and temperature. The statistics were obtained from more than 300 NCs including all shapes for each sample.

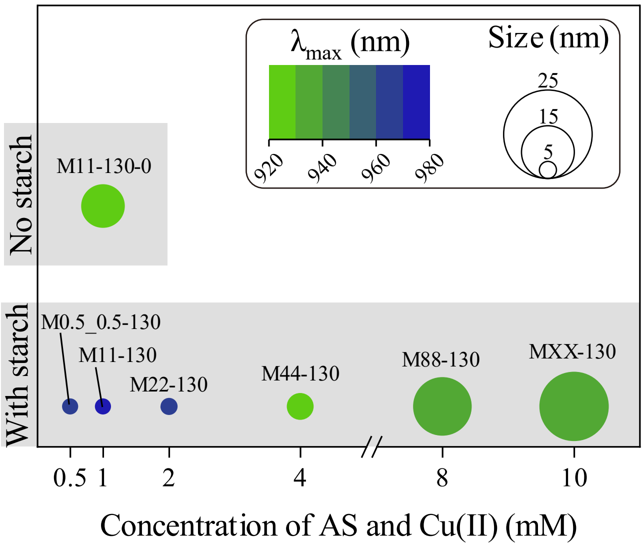

Figure S3. Size distribution summary of CuS NCs synthesized with different concentrations of ammonium sulfide (AS) and Cu(II), and with or without starch. The size is equivalent to the average diameter of CuS NCs observed in TEM (i.e., the lateral dimension of the NCs), which is obtained from the fitting of the corresponding crystal size distribution (Figure S4). The values of λ_{max} are derived from UV-vis spectra discussed in the following.

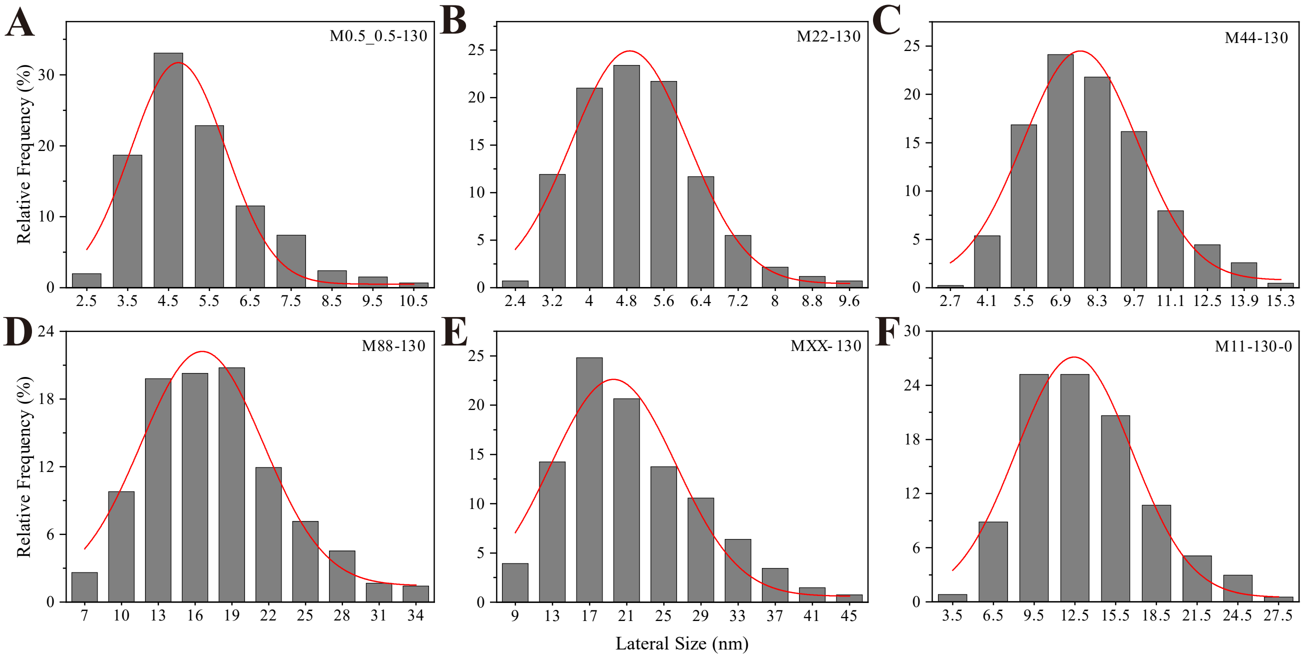

Figure S4. Size distribution of CuS NCs with different Cu and AS concentrations, and with the absence of starch in synthesis. M11-130 is presented in Figure S2F. The statistics were obtained from more than 300 NCs including all shapes for each sample.

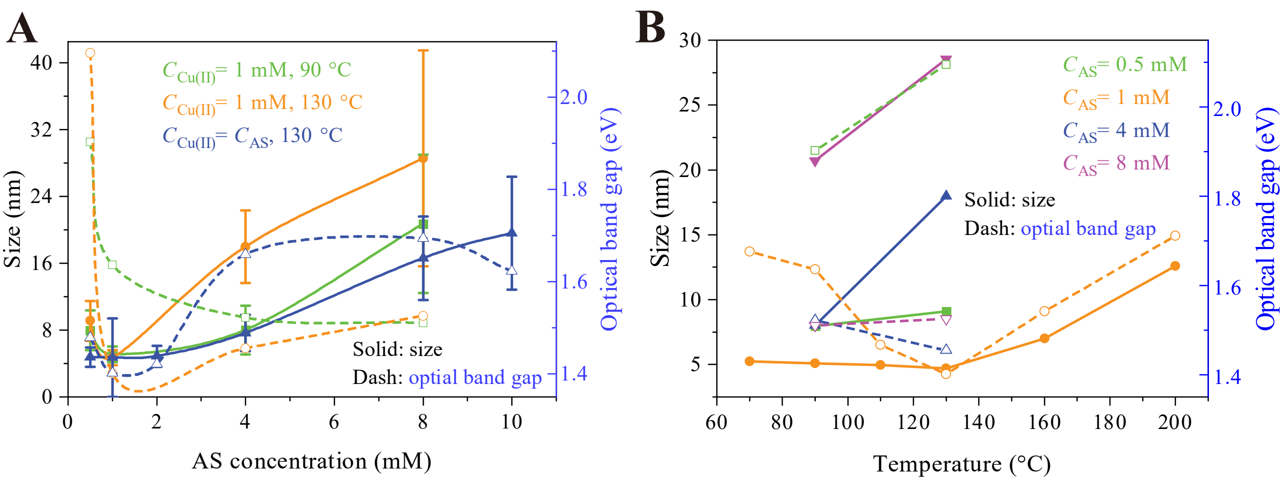

Figure S5. (A) The size and optical band gap of CuS NCs synthesized at (A) different precursor concentrations and (B) temperature. Error bars in (A) indicate standard deviations (σ from the Gauss fitting of the size distribution), which are not included in (B) for clarity. Cu(II) concentration in (B) is 1 mM.

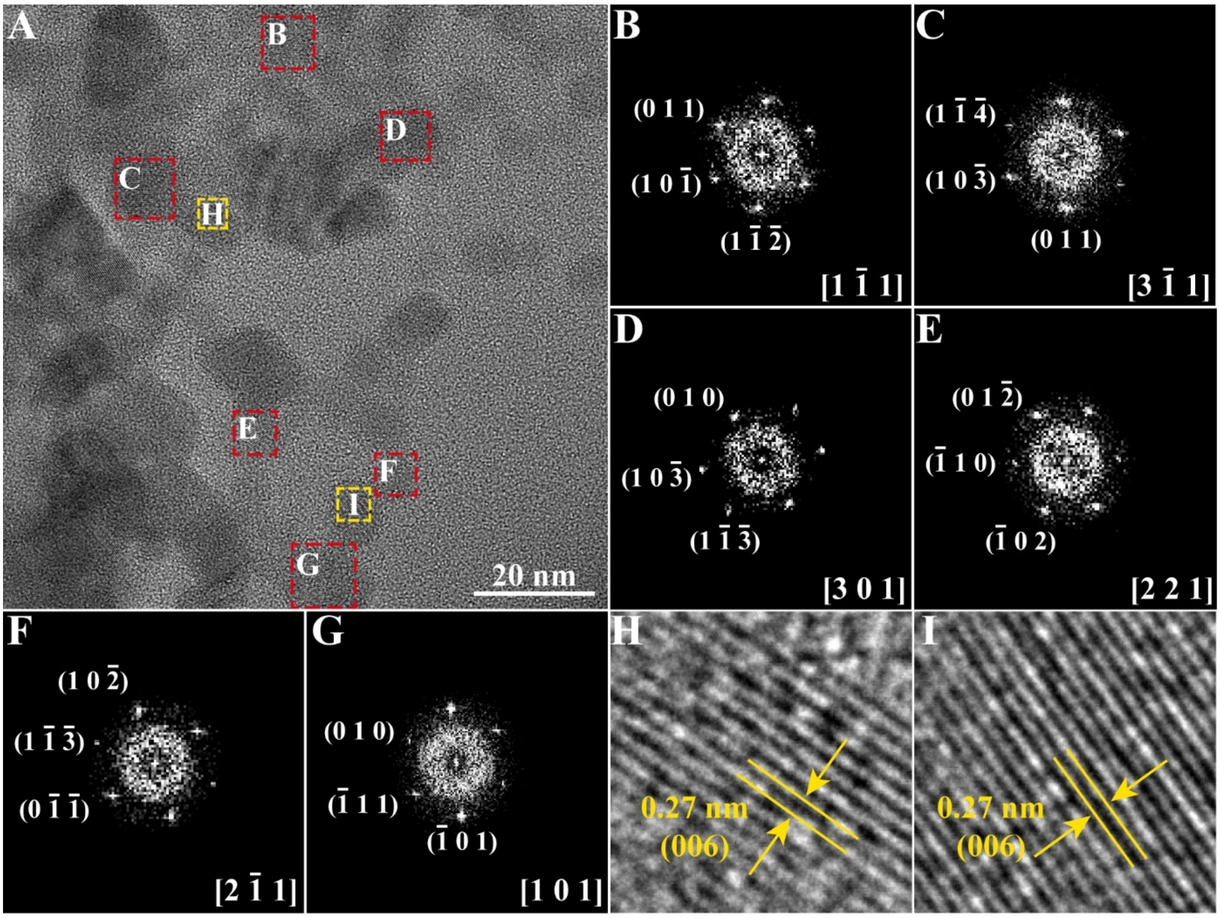

Figure S6. Orientation of small CuS NCs without starch coating. (A) TEM image of small CuS NCs without starch coating. (B)–(G) Fast Fourier transform of the individual NCs marked by the red squares in (A), showing their zone axes. (H)–(I) HRTEM of individual NCs marked by the yellow squares in (A) show lattice spacings of 0.27 nm attributed to (006).

Table S1. Angles (°) between the zone axes observed in Figure S5.

Observed zone axes	$[1\bar{1}1]$	$[3\bar{1}1]$	[301]	[221]	$[2\bar{1}1]$	[101]
$[1\bar{1}1]$	0	19.7	18.9	32.7	10.8	12.4
$[3\bar{1}1]$	19.7	0	9.8	39.6	8.9	27.4
[301]	18.9	9.8	0	30.1	10.9	21.8
[221]	32.7	39.6	30.1	0	35.4	21.4
$[2\bar{1}1]$	10.8	8.9	10.9	35.4	0	19.6
[101]	12.4	27.4	21.8	21.4	19.6	0
Average ± SD[a)]	18.9 ± 8.6	21.1 ± 12.8	18.3 ± 8.3	31.8 ± 6.8	17.1 ± 11.0	20.5 ± 5.4

[a)] SD: standard deviation. The value of zero (angle between the same zone axis) is excluded when calculating average and SD.

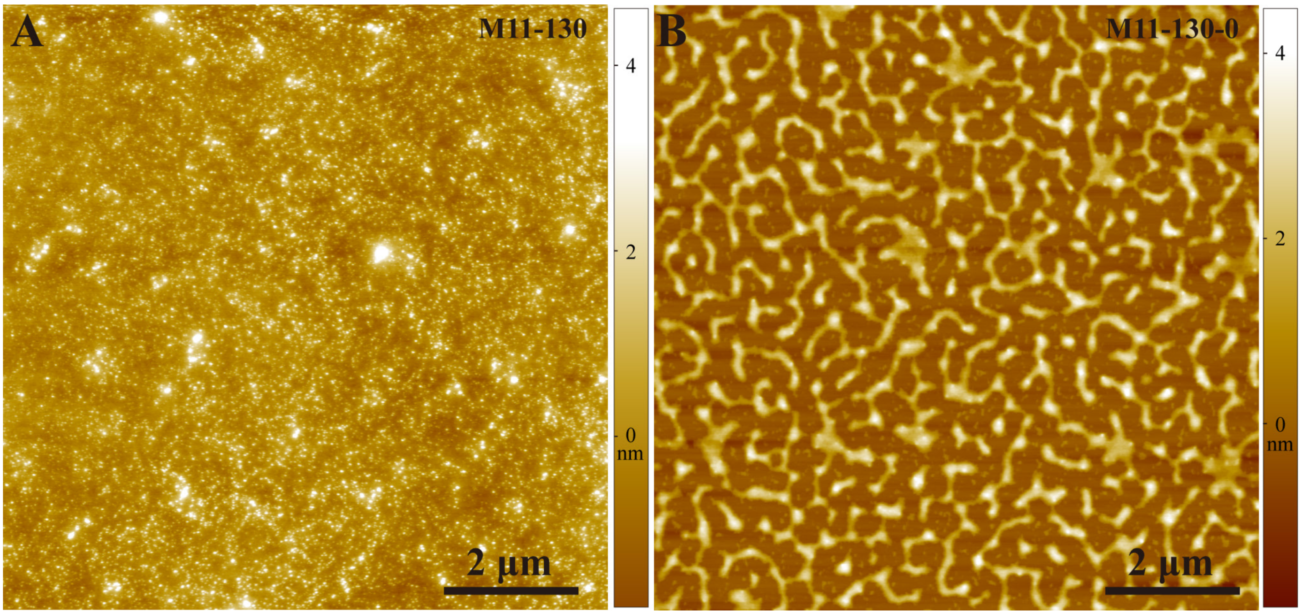

Figure S7. Concentrated CuS NCs dried on mica wafer. (A) M11-130 is homogeneously distributed on a mica wafer. (B) M11-130-0 aggregates on a mica wafer and forms islands.

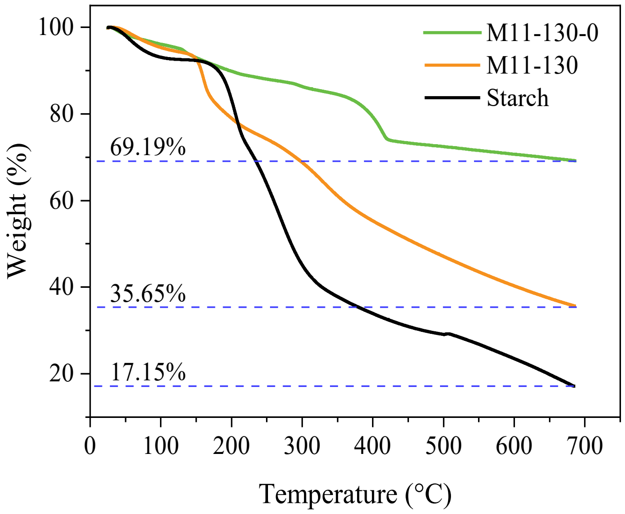

Figure S8. TGA curves of M11-130-0, M11-130, and starch from room temperature to 700 °C in N_2.

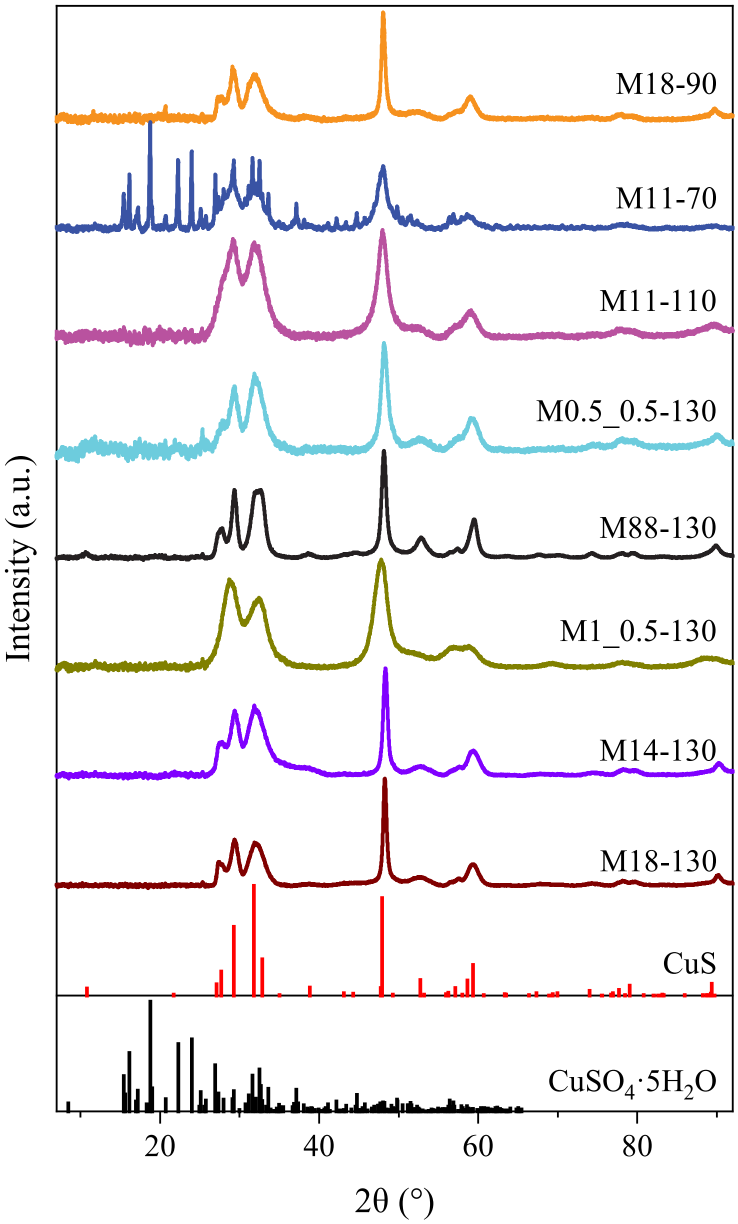

Figure S9. XRD patterns of CuS NCs synthesized with starch under typical experimental conditions. The reference patterns are CuS (COD 96-900-0524, COD ID: 9000523) and $CuSO_4 \cdot 5H_2O$ (ICOD 01-072-2355).

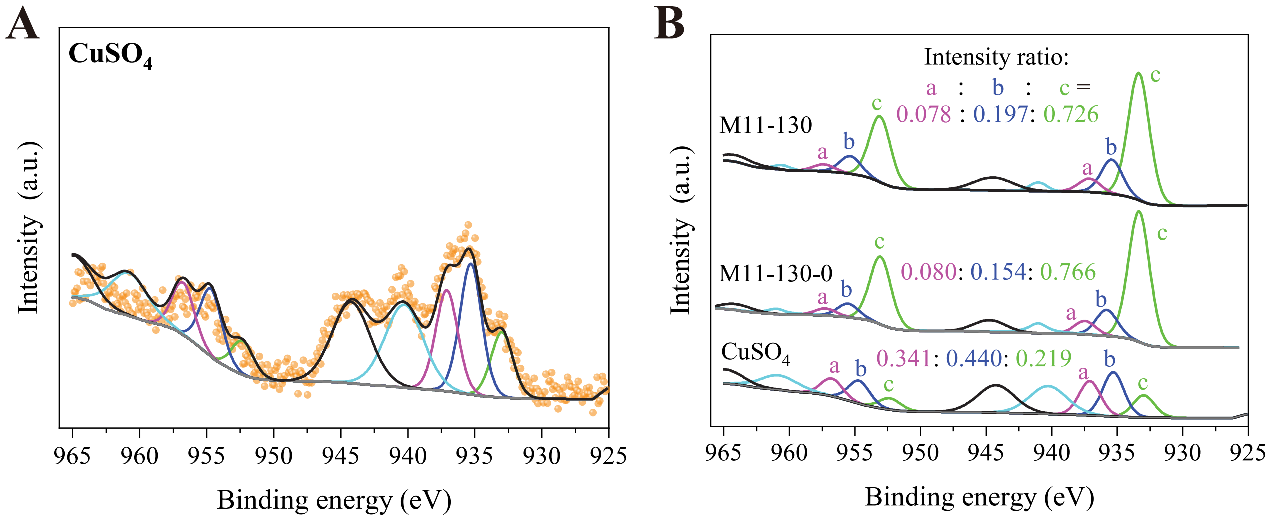

Figure S10. XPS spectra comparison of CuSO$_4$ and CuS NCs. (A) High-resolution Cu 2p XPS of CuSO$_4$. (B) Comparison of high-resolution Cu 2p XPS of M11-130, M11-130-0, and CuSO$_4$. Included are the intensity ratios of the three main pairs of Cu 2p$_{1/2}$ and Cu 2p$_{3/2}$ peaks.

Table S2. Angles (°) between zone axes observed and potential zone axes of small CuS NCs.

Observed zone axes	Potential zone axes			
	$[001]$	$[100]$	$[010]$	$[110]$
$[1\bar{1}1]$	21.9	71.2	108.8	90
$[3\bar{1}1]$	39.9	51.5	116.4	79.8
$[301]$	34.8	55.2	106.6	73.4
$[221]$	24.9	77.9	77.9	65.1
$[2\bar{1}1]$	31.5	60.4	113.3	84.3
$[101]$	13.1	76.9	96.5	83.5
Average ± SD	27.7 ± 9.7	65.5 ± 11.4	103.3 ± 14.2	79.4 ± 8.9

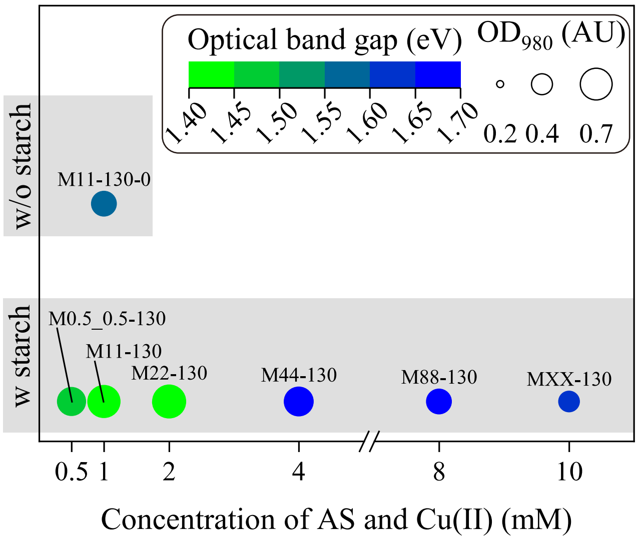

Figure S11. Summary of UV-vis spectra of CuS NCs synthesized with different concentrations of AS and Cu(II), and with or without starch. Refer to Figure S15 for detailed spectra.

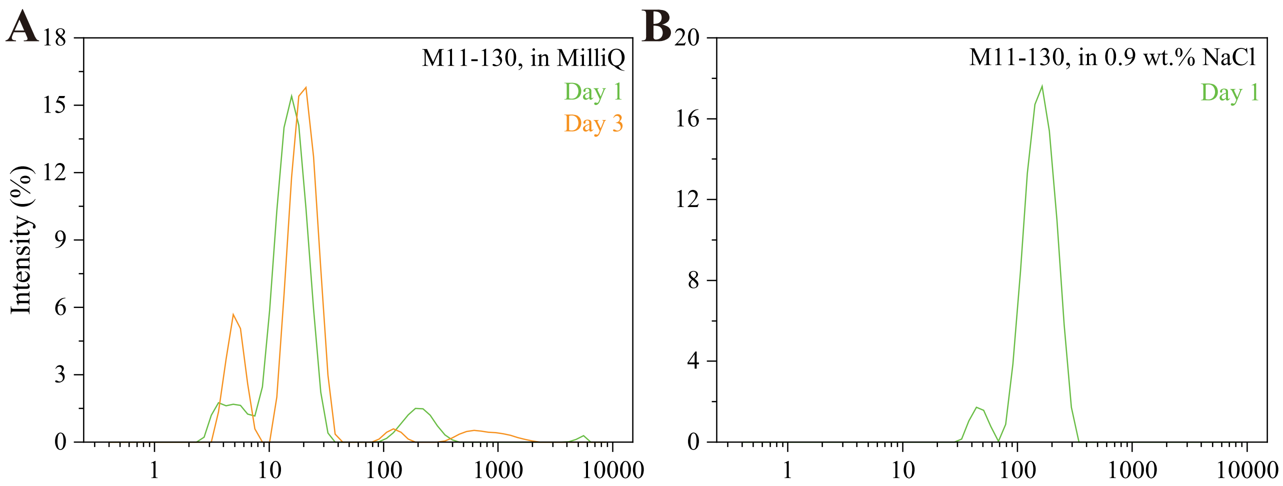

Figure S12. Hydrodynamic size of M11-130 determined using dynamic light scattering. Average hydrodynamic size distribution of M11-130 in (A) MilliQ water and (B) 0.9 wt.% NaCl solution. On Day 3, precipitation was observed for M11-130 in 0.9 wt.% NaCl solution. The CuS NCs solution was stored at room temperature.

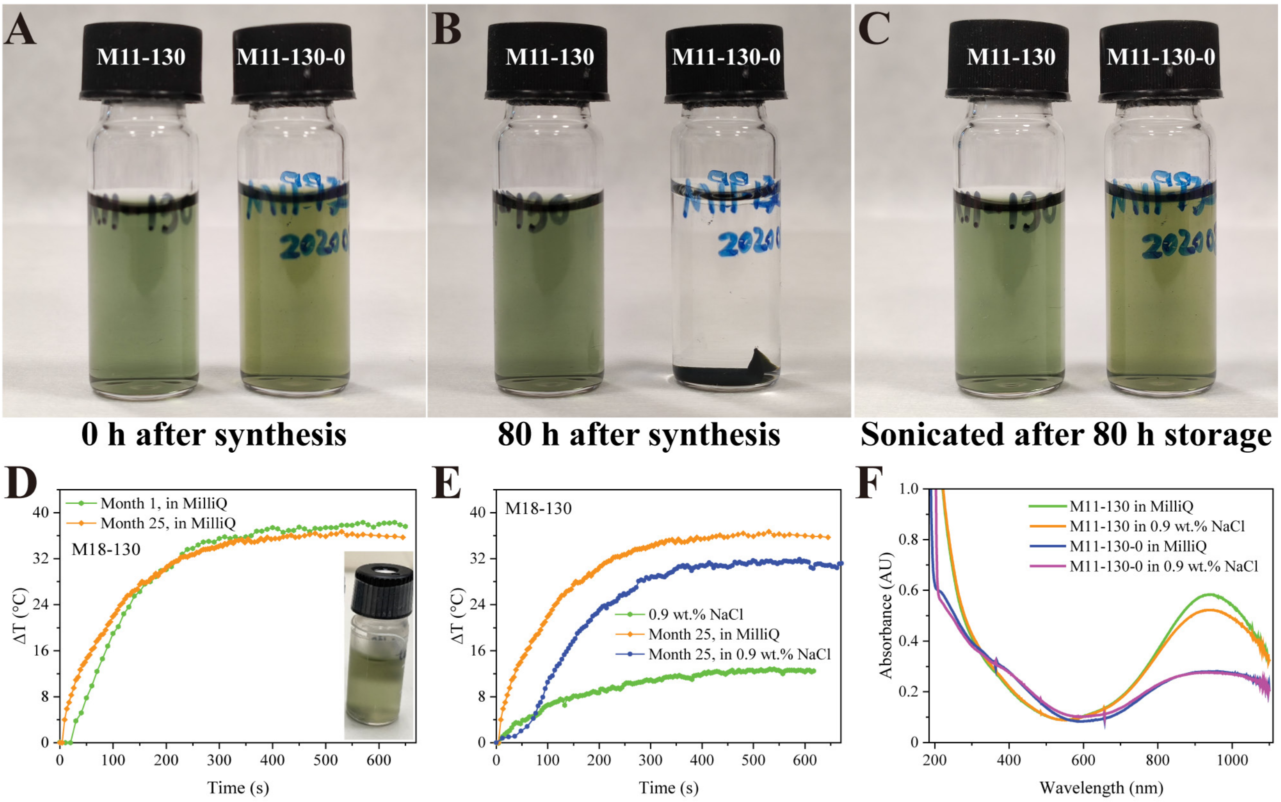

Figure S13. Stability of CuS NCs. (A) After synthesis, both M11-130 and M11-130-0 are homogenous solutions. (B) After being stored for 80 h at 4 °C, M11-130 remains a solution while M11-130-0 aggregates and forms film. (C) After sonicated for 30 s, no apparent change was observed in M11-130, while M11-130-0 returns as a solution. (D) M18-130 remained homogenous green solution and retained photothermal activity after 25 months storage in aqueous solution at 4 °C. (E) Temperature curves of M18-130 in Month 25 in MilliQ water and 0.9 wt.% NaCl. (F) UV-vis spectra of M11-130 and M11-130-0 in MilliQ water and 0.9 wt.% NaCl.

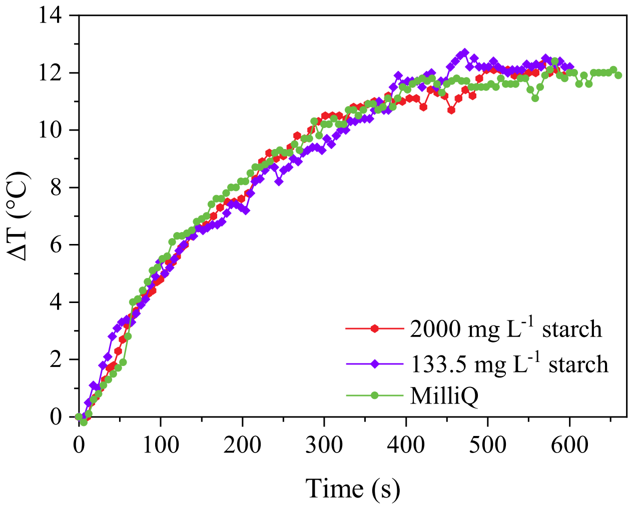

Figure S14. The photothermal effect of starch solutions in response to 980 nm laser illumination. Starch does not have any photothermal activity responding to 980 nm laser since its water solutions show the same temperature response as MilliQ water. Starch of 133.5 mg L^{-1} is the amount of the starch in 50 mg L^{-1} M11-130, and 2000 mg L^{-1} starch was used in the synthesis of M11-130. MilliQ water was used as a control.

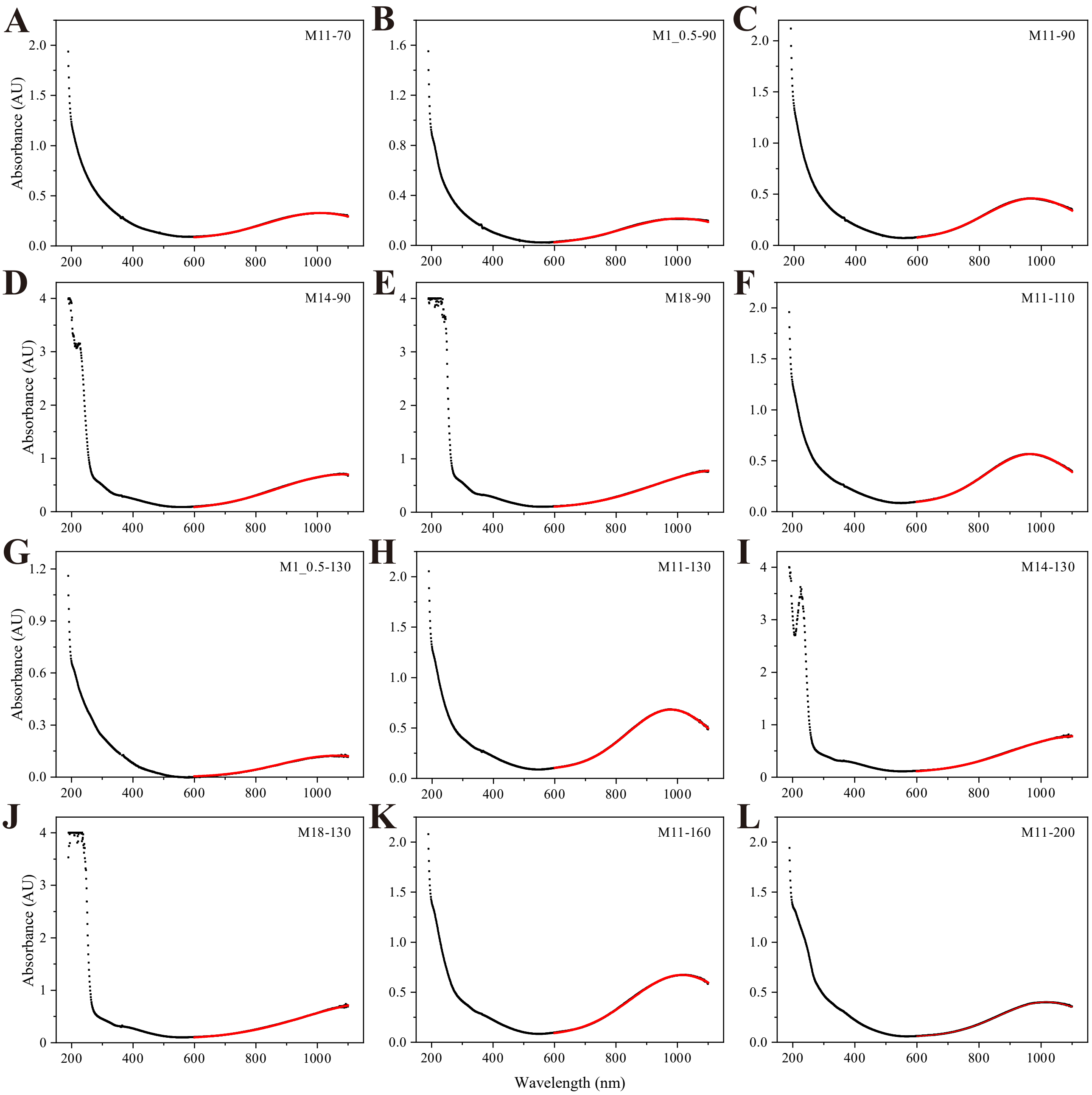

Figure S15. UV-vis spectra of CuS NCs synthesized with different concentrations of AS and temperature. The samples were normalized to equal initial Cu(II) concentrations. Data between 600 to 1100 nm were fitted using Gauss fitting to find the wavelength of maximum absorbance (λ_{max}).

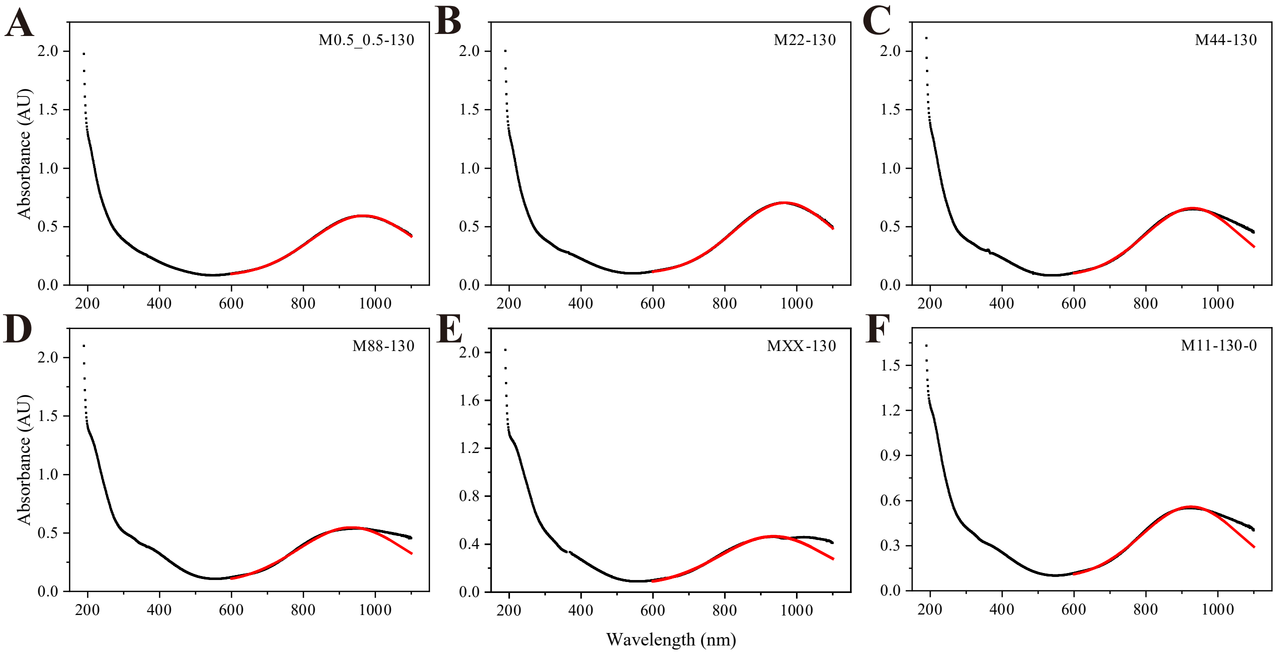

Figure S16. UV-vis spectra of CuS NCs with different Cu and AS concentrations, and with no starch in the synthesis. The Gauss fitting of M44-130, M88-130, MXX-130, and M11-130-0 is poor in the 600-1100 nm range and the range is adjusted to 600 to 1000 nm.

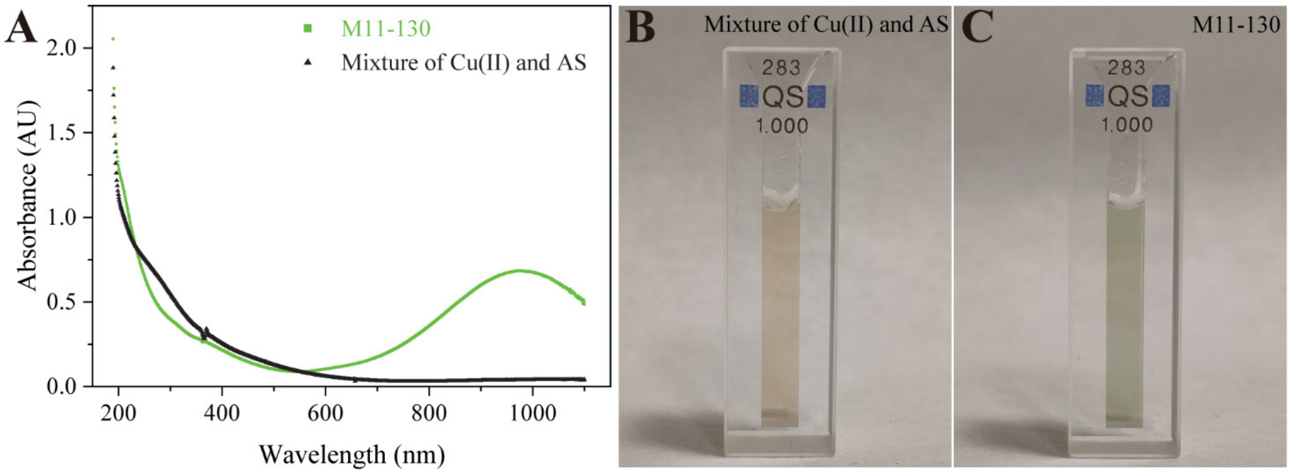

Figure S17. Comparison of typical CuS NCs and the mixture of Cu(II) and AS (precursors). (A) UV-vis spectra of M11-130 and the mixture of Cu(II) and AS. Digital picture of (B) the mixture of Cu(II) and AS and (C) M11-130. The initial concentration of Cu was diluted to 0.2 mM.

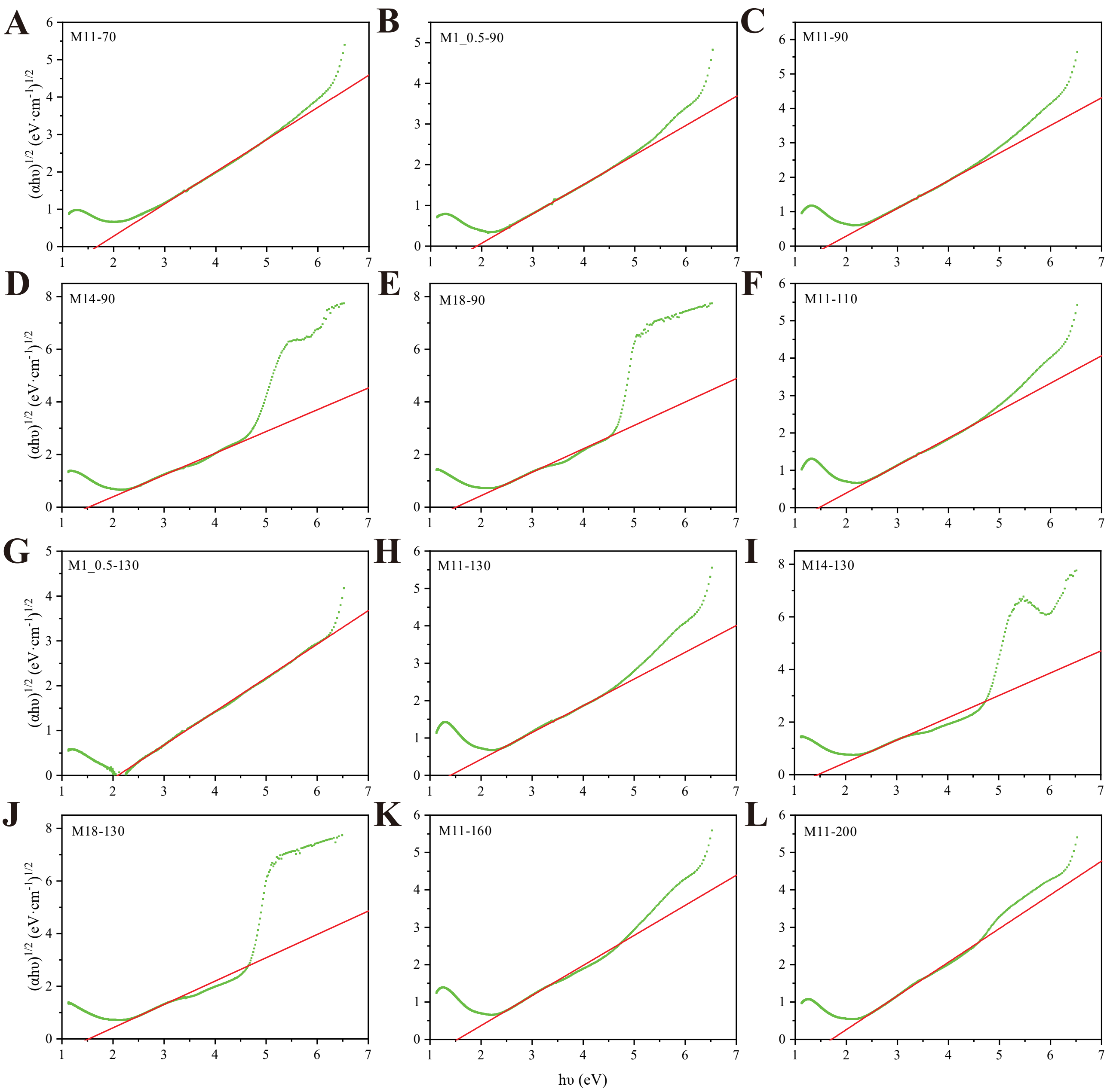

Figure S18. Optical band gap of CuS NCs synthesized with different concentrations of AS and temperature. The value of the intercept of the *x*-axis (y=0) is the optical band gap.

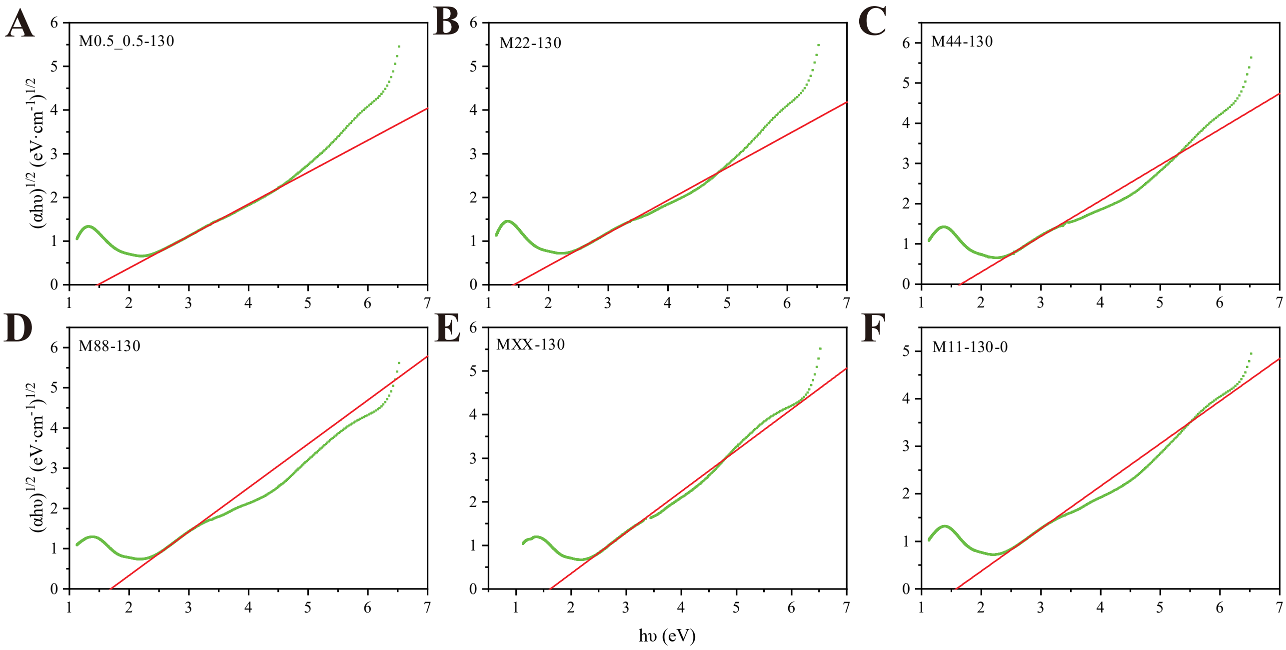

Figure S19. Optical band gap of CuS NCs with different Cu and AS concentrations, and with the absence of starch in synthesis. The value of the intercept of the *x*-axis (y=0) is the optical band gap.

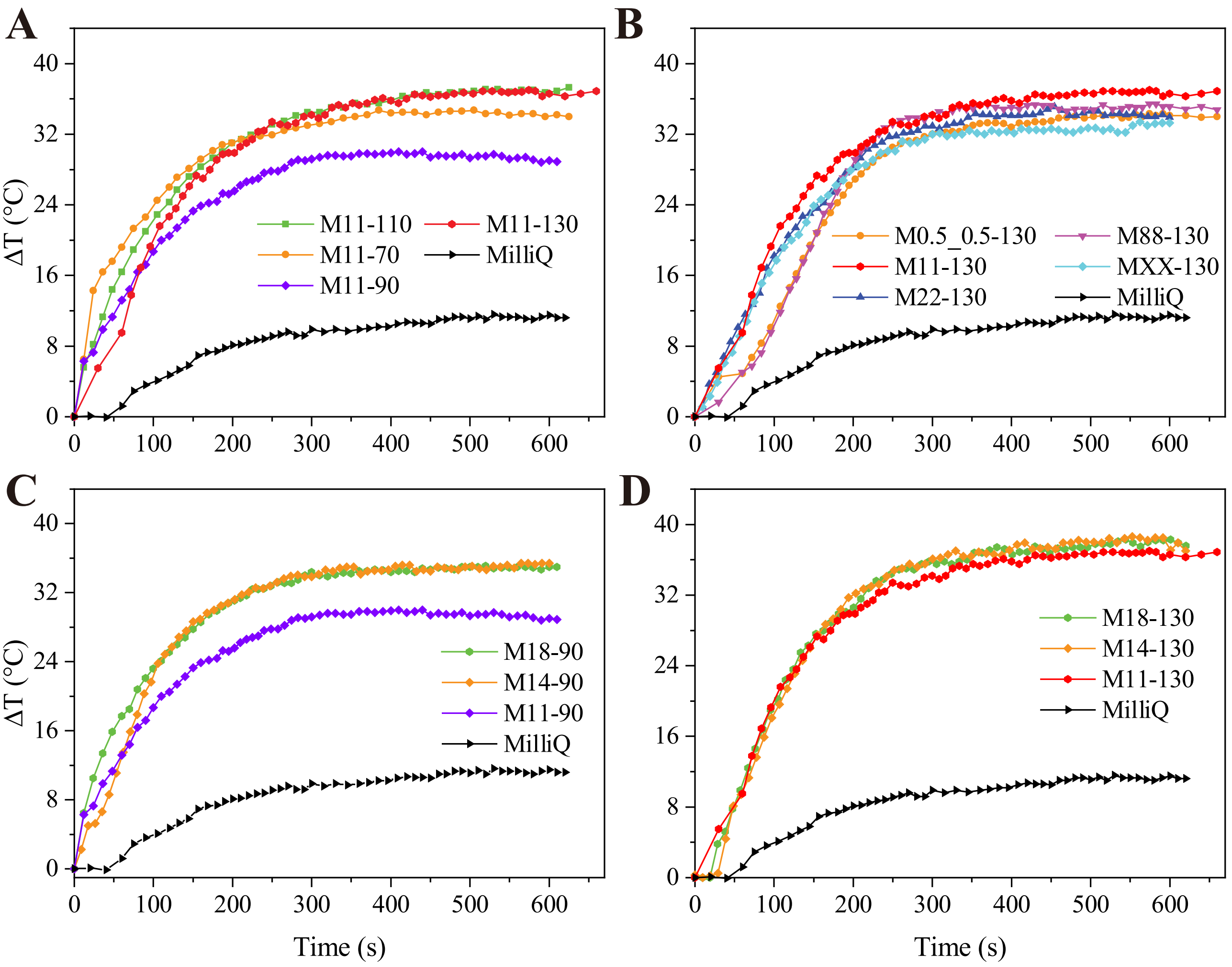

Figure S20. The temperature curves of CuS NCs synthesized (A) at different temperatures, (B) with different Cu(II) and AS concentrations, and different ratios of Cu(II) and AS at (C) 90 °C and (D) 130 °C. CuS NCs were prepared in 0.5 mL MilliQ water at 50 mg L^{-1} Cu concentration. Some plots were duplicated for comparison.

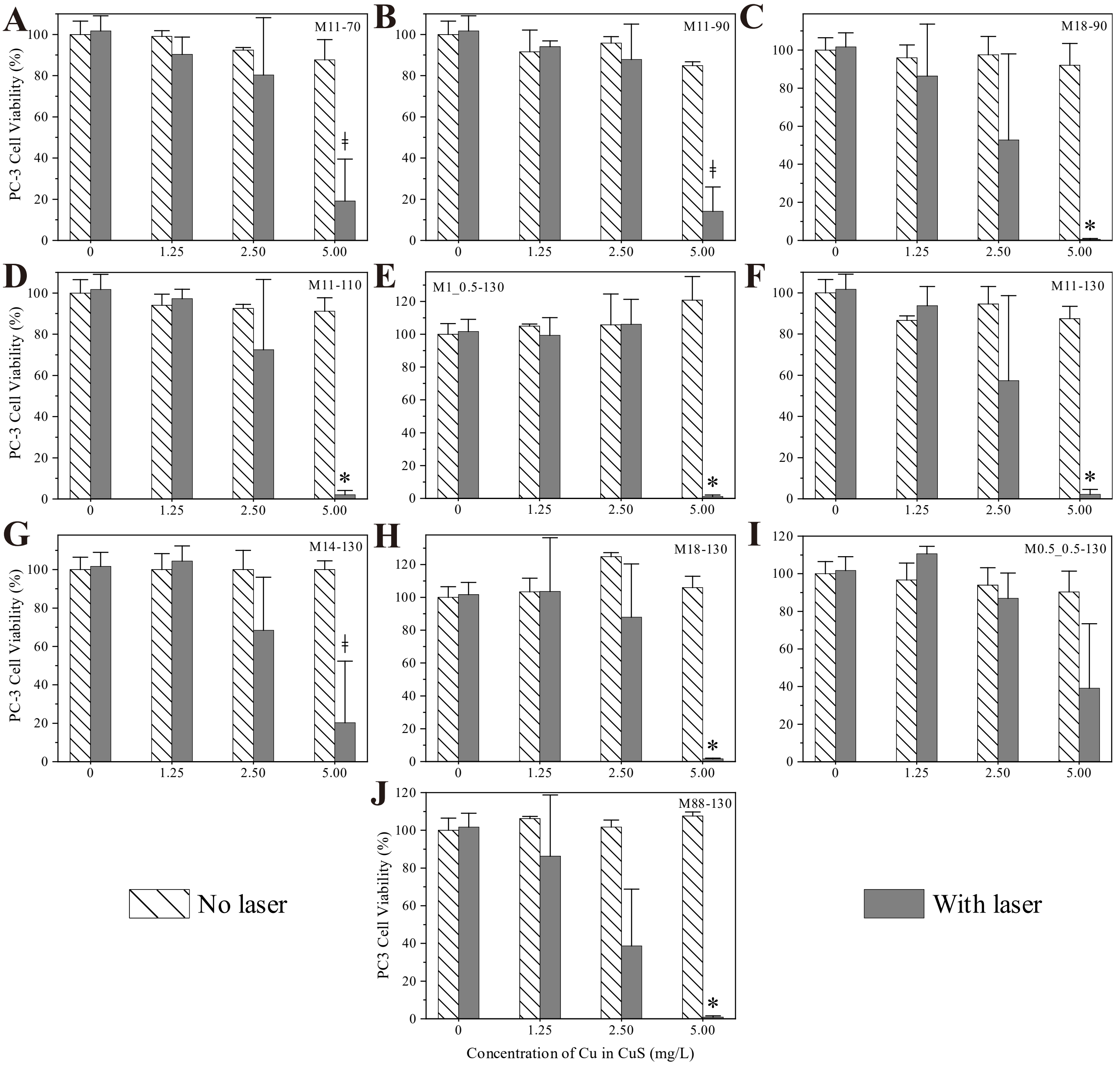

Figure S21. Detailed photothermal ablation of PC-3/Luc+ cancer cells by different CuS NCs. Cell viability after treatment by (A) M11-70, (B) M11-90, (C) M18-90, (D) M11-110, (E) M1_0.5-130, (F) M11-130, (G) M14-130, (H) M18-130, (I) M0.5_0.5-130, and (J) M88-130 at 0, 1.25, 2.5, and 5.0 mg L^{-1} Cu with and without laser. * $p < 0.0002$, ǂ $p < 0.006$ compared to the control experiments.

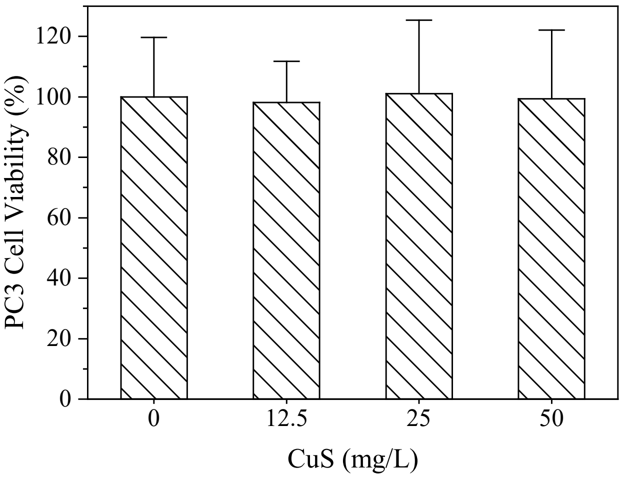

Figure S22. Typical cytotoxicity of starch-coated CuS NCs to PC-3/Luc+ cells after 24 h treatment by different concentrations of CuS NCs. The cell viabilities of the CuS NCs treated cells are comparable to the control cells without any CuS NCs, $p > 0.2$.

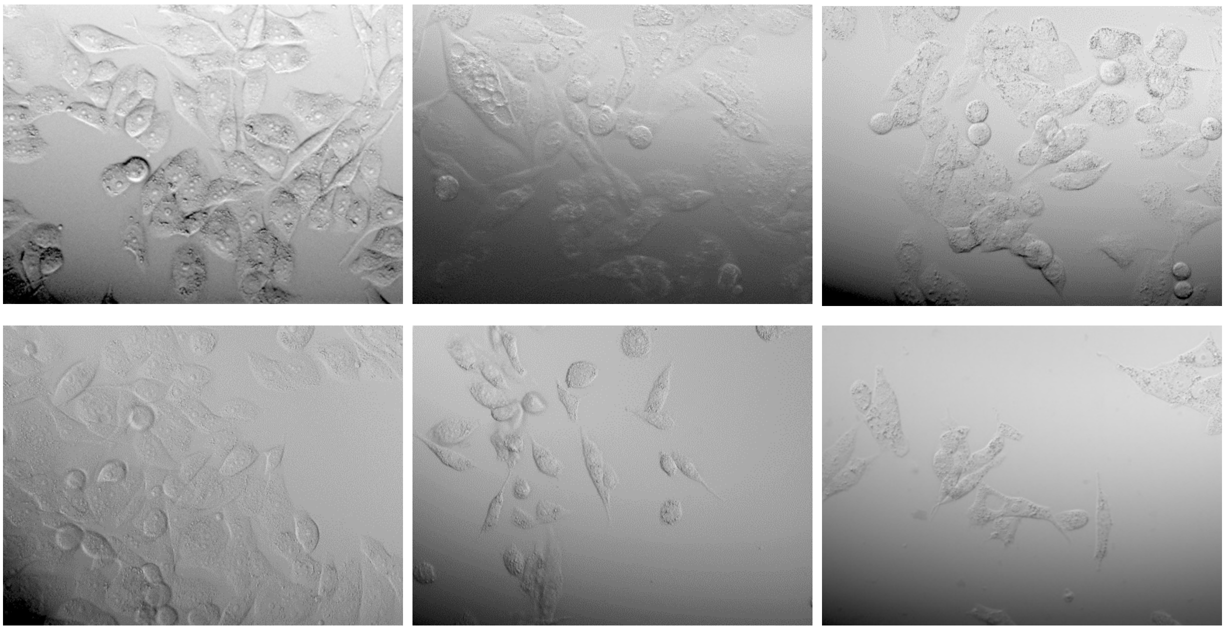

Figure S23. In vitro cell morphology. Microscopic images show the morphology of PC-3/Luc+ cells after M11-130 treatment. From left column to right column: 0, 10, and 20 mg L^{-1} CuS NCs. Top row: without laser treatment. Bottom row: with laser treatment.

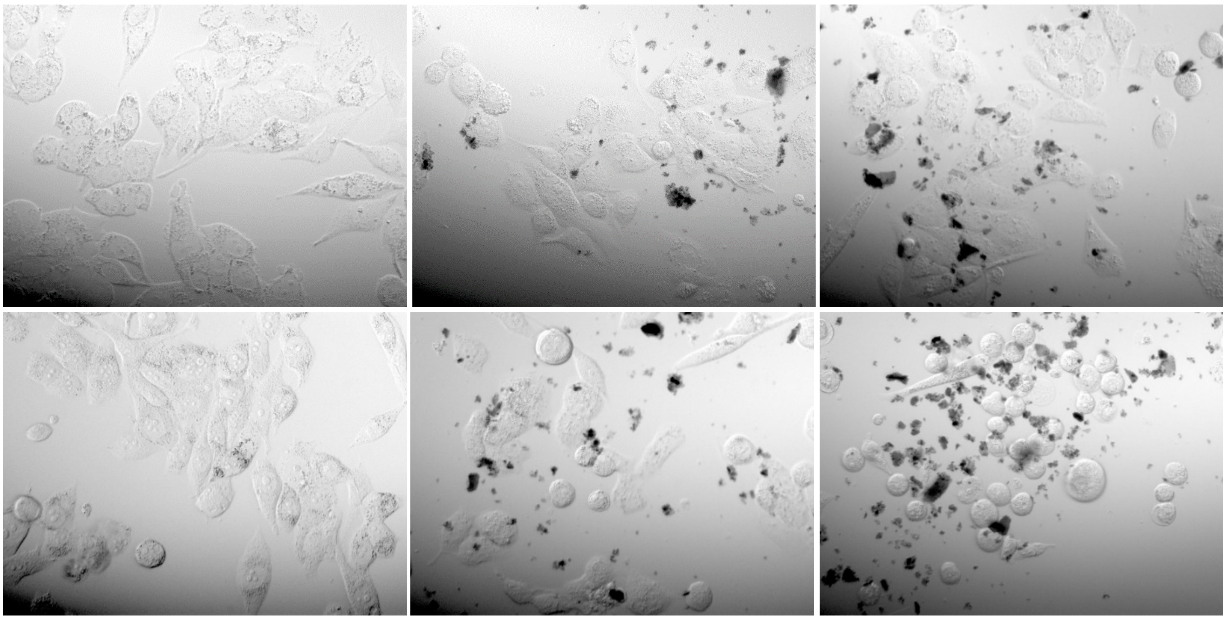

Figure S24. In vitro cell morphology. Microscopic images show the morphology of PC-3/Luc+ cells after M11-130-0 treatment. From left column to right column: 0, 10, and 20 mg L^{-1} CuS NCs. Top row: without laser treatment. Bottom row: with laser treatment.

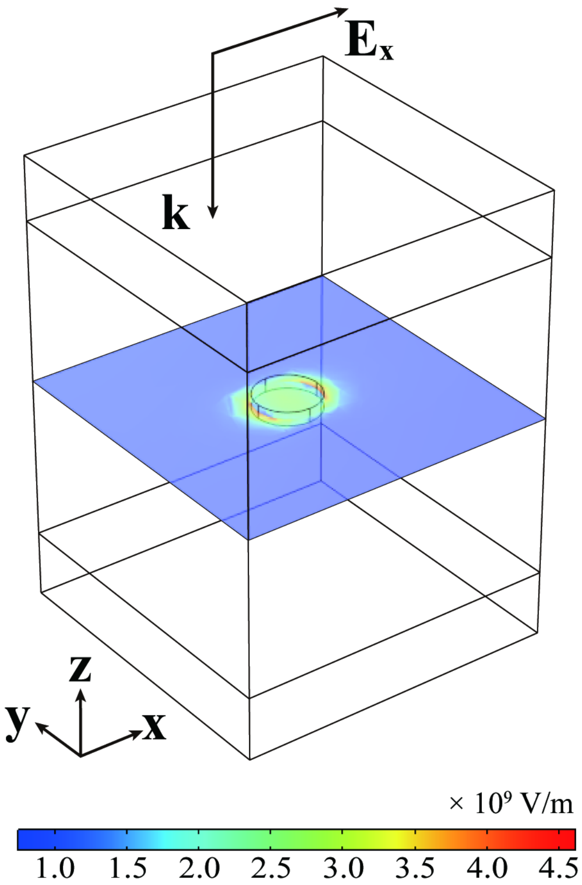

Figure S25. Computational domain and **E** field analysis of a CuS NC with in-plane LSPR mode. The wavelength shown is 980 nm and the particle is M11-130.

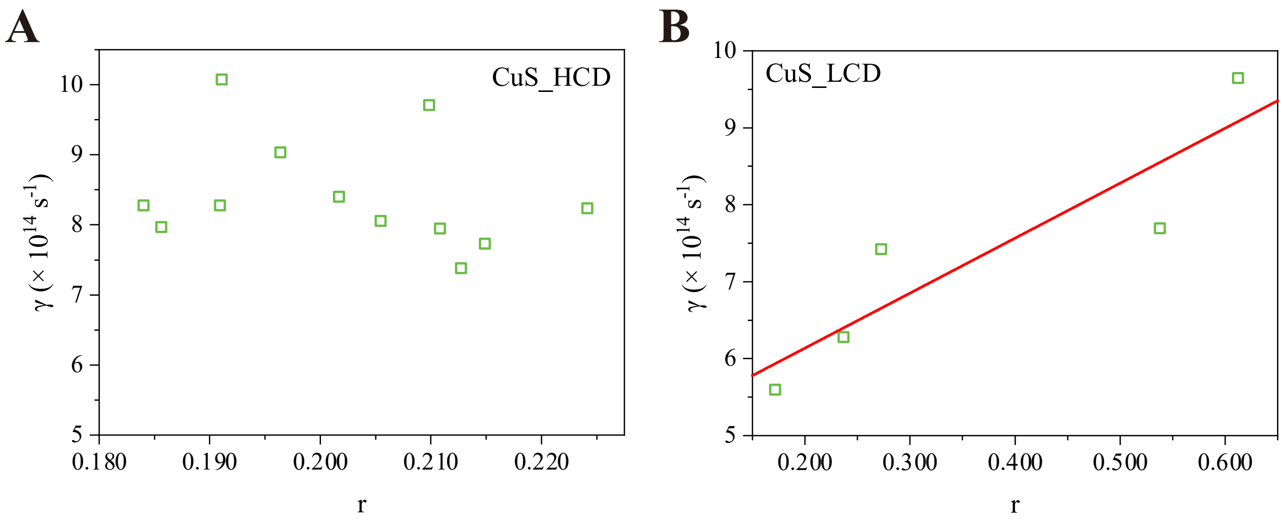

Figure S26. Effect of aspect ratio *r* (= height/diameter) on the damping constants of (A) CuS_HCD and (B) CuS_LCD.

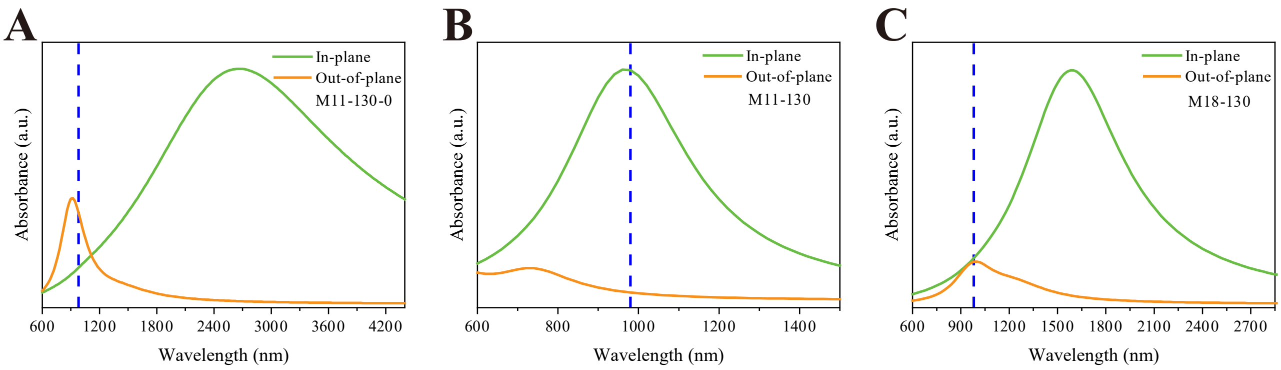

Figure S27. Spectra simulation with complete in-plane and out-of-plane LSPR. The blue lines indicate the position of 980 nm.

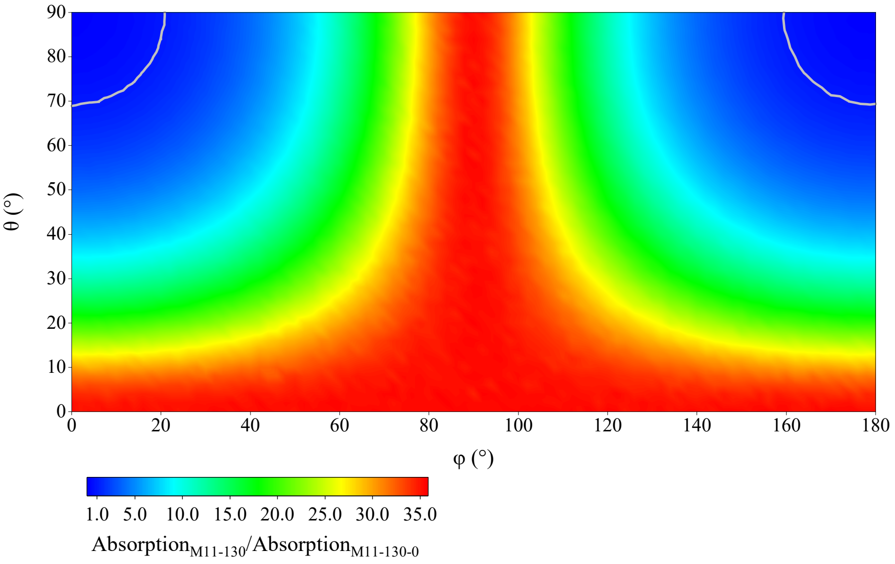

Figure S28. Absorption gain at 980 nm wavelength of M11-130 over M11-130-0 at different orientations. The two quarter-circle areas at upper corners indicate gains smaller than unity, which accounts for about 4% of orientations.

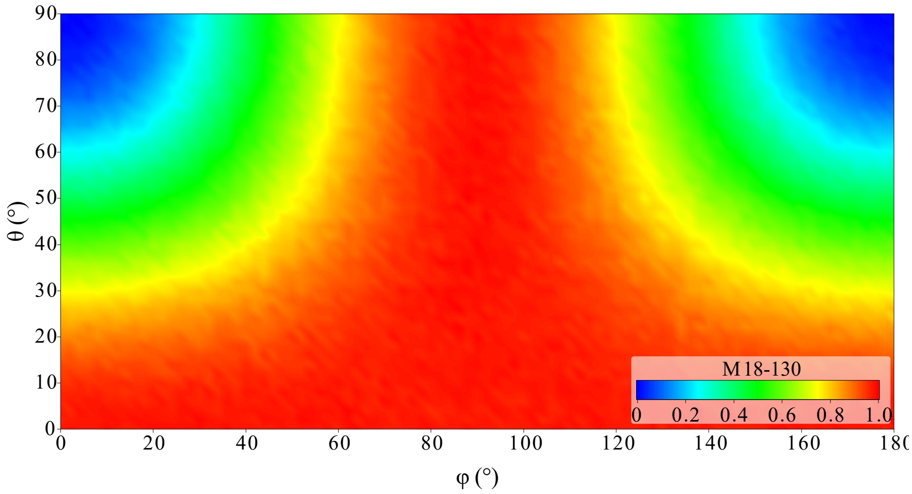

Figure S29. The effect of particle orientation (θ and φ) on the normalized absorption at 980 nm of M18-130.

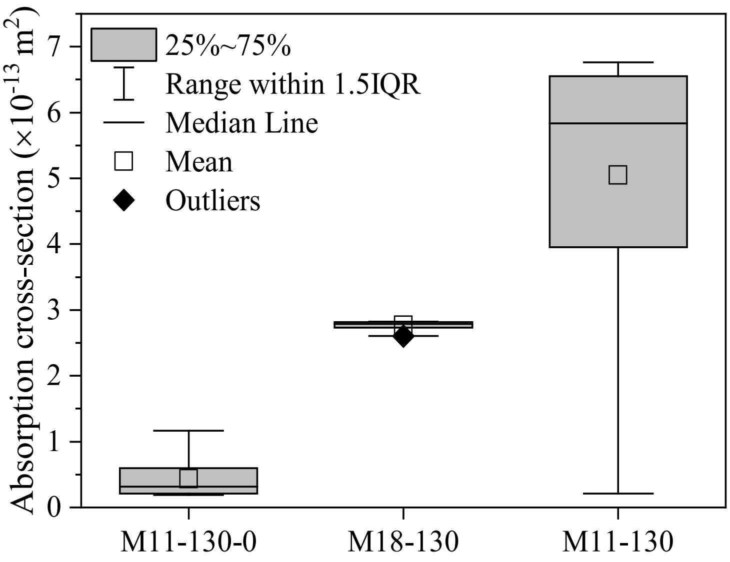

Figure S30. Absorption cross-section of M11-130-0, M18-130, and M11-130, represented by statistical distributions from all orientations in Figure 6E, Figure 6G, and Figure S29. IQR: interquartile range.

Supporting References

[1] J. Kundu, D. Pradhan, *ACS Appl. Mater. Interfaces* **2014**, *6*, 1823.

[2] E. Güneri, A. Kariper, *J. Alloys Compd.* **2012**, *516*, 20.

[3] X. Li, Y. Li, F. Xie, W. Li, W. Li, M. Chen, Y. Zhao, *RSC Adv.* **2015**, *5*, 84465.

[4] J. Tauc, R. Grigorovici, A. Vancu, *Phys. Status Solidi B* **1966**, *15*, 627.

[5] K. Baishya, J. S. Ray, P. Dutta, P. P. Das, S. K. Das, *Appl. Phys. A: Mater. Sci. Process.* **2018**, *124*, 704.